

Airborne Dual-Doppler Observations of an Intense Frontal System Approaching the Pacific Northwest Coast

SCOTT A. BRAUN*

National Center for Atmospheric Research,⁺ Boulder, Colorado

ROBERT A. HOUZE JR.

Department of Atmospheric Sciences, University of Washington, Seattle, Washington

BRADLEY F. SMULL

NOAA/ERL/National Severe Storms Laboratory, Boulder, Colorado, and Department of Atmospheric Science, University of Washington, Seattle, Washington

(Manuscript received 24 September 1996, in final form 7 May 1997)

ABSTRACT

Airborne Doppler radar data, collected off the Pacific Northwest coast by a NOAA WP-3D Orion aircraft over an 8-h period on 8 December 1993 during the Coastal Observations and Simulations with Topography experiment, reveal the mesoscale structure of an intense frontal system while it was well offshore and as it approached within 20 km of the Oregon coastline. During the offshore stage, a portion of the narrow cold-frontal rainband was characterized by deep convective cores. Pseudo-dual-Doppler analyses characterize the kinematic and precipitation structure of the deep convection.

Pseudo-dual-Doppler analyses describe the subsequent evolution of the narrow cold-frontal rainband as it approached to within 20 km of the Oregon coast. Deformation of the frontal zone appeared to cause the dissipation of one of three precipitation cores contained within the dual-Doppler area. The precipitation cores and the strong convergence zone associated with the front conformed to some degree to the shape of the coastline near Cape Blanco, Oregon, as the front neared the coast. Changes in the prefrontal flow that occurred as the front approached the coast were qualitatively consistent with theoretical and numerical studies of upstream orographic influence. Comparison of pseudo-dual-Doppler-derived velocity profiles with idealized numerical model calculations suggests that the nearshore evolution of the frontal rainband was significantly affected by an upstream influence of the coastal orography.

1. Introduction

The growing concentration of population, commerce, and transportation along the coastal margins of North America has rendered our society increasingly vulnerable to the vagaries of coastal meteorology. While extreme cyclones, producing surface gusts in excess of 40 m s⁻¹, are relatively infrequent along the western coast of the United States, more ordinary cyclonic storms often produce locally strong winds and occasional se-

vere weather including floods and mudslides. The highly variable (and thus typically undersampled) nature of coastal circulations, as well as their poor representation in forecast models, have hindered progress in this area of growing scientific interest and practical importance.

In response to the lack of data in coastal regions, the first field phase of the Coastal Observations and Simulations with Topography (COAST) experiment was conducted 30 November–15 December 1993 along the Pacific Northwest coast of North America. The project was designed to collect those special observations necessary to document, and ultimately anticipate, the influence of orography on mesoscale (10–500 km) weather phenomena in coastal environments. A key goal was to observe the mesoscale structure of fronts and other features associated with baroclinic cyclones over the open sea and describe their modification as they came under the influence of orography.

This study describes pseudo-dual-Doppler (hereafter referred to simply as dual-Doppler) radar data and flight-

* Current affiliation: Universities Space Research Association, Sea-
brook, Maryland.

⁺ The National Center for Atmospheric Research is sponsored by
the National Science Foundation.

Corresponding author address: Dr. Scott A. Braun, Mesoscale At-
mospheric Processes Branch, NASA/GSFC, Code 912, Greenbelt, MD
20771.

E-mail: braun@gilbert.gsfc.nasa.gov

level observations from a National Oceanographic and Atmospheric Administration (NOAA) WP-3D Lockheed Orion (P-3) aircraft during the third intensive operations period (IOP 3) of COAST on 8 December 1993, during which cold-frontal rainbands were sampled by aircraft far offshore and then again in the coastal zone of Oregon. The cold-frontal bands were associated with a rapidly developing cyclone that reached maturity near the Pacific Northwest coast. During the developing stage of the cyclone of 8 December 1993, while the front was far from the coast, a portion of the narrow cold-frontal rainband (NCFR) consisted of a line of intense, deep convection, but near the coast, this storm system exhibited a NCFR structure similar to previously observed cold fronts [i.e., a shallower zigzag pattern of precipitation cores and gap regions (Hobbs and Biswas 1979; James and Browning 1979)].

In this paper, we focus first on the deep convection that formed along a portion of the NCFR well out to sea. The Doppler data collected during this offshore phase are unique in documenting the kinematic structure of deep convection along the cold front of a developing oceanic cyclonic system. For the nearshore phase of the flight, we focus on the structure and evolution of the NCFR in the coastal zone and the possible modification of the rainband by the upstream influence of the steep coastal orography.

Kinematic and precipitation structures of fronts were studied previously in the Pacific Northwest (Nagle and Serebreny 1962; Houze et al. 1976; Hobbs et al. 1980; Matejka et al. 1980; Hobbs and Persson 1982) and near Great Britain (Browning and Harrold 1970; Browning 1971; Browning and Pardoe 1973; James and Browning 1979). These studies employed radars, rawinsondes, and aircraft instrumented for cloud microphysical research. They identified and classified rainband structures associated with warm, cold, and occluded fronts and described the kinematic and microphysical characteristics of the rainbands. Some interactions of these bands with orography have been described by Browning et al. (1974), Hobbs et al. (1975), Hill et al. (1981), and Parsons and Hobbs (1983a).

These previous studies relied heavily on land-based single-Doppler radar observations. Reported dual-Doppler results were confined to rather benign frontal situations (Hertzman et al. 1988). Though informative, single-Doppler data (e.g., Browning and Harrold 1970; Hobbs et al. 1980; Matejka et al. 1980; Hobbs and Persson 1982) are inadequate to specify uniquely the rotational and vertical circulations along fronts. Furthermore, these studies were confined to storms typically in their mature stages and already under the influence of orography. Therefore, they could not describe the full space- and time-dependent nature of these systems.

Carbone (1982) examined a NCFR in the Central Valley of California by means of land-based triple-Doppler radar. This NCFR was accompanied by strong winds, lightning, and brief tornadoes and had updrafts of 15–

20 m s⁻¹. The role of the local orography was not examined. Roux et al. (1993) documented a less intense landfalling NCFR over northwestern France by means of dual-Doppler radar. Roux et al. (1993) and Merécal et al. (1993) applied retrieval techniques to diagnose the thermodynamic and microphysical structures of the NCFR, but owing to relatively flat coastal terrain, they could not examine strong coastal effects such as those that occur on the west coast of North America.

Research aircraft equipped to collect a combination of in situ and remote measurements are, at present, the only practical means to document three-dimensional airflow and precipitation structure over rugged coastal terrain and well offshore. Several previous programs have used aircraft in the study of cyclonic storms over the oceans but in ways quite distinct from COAST. For example, in the 1980 Storm Transfer and Response Experiment (Bond and Fleagle 1988) and the 1987 Ocean Storms Project (Bond and Shapiro 1991), aircraft collected flight-level data within cyclonic storms over the northeastern Pacific Ocean, but no Doppler radar data were obtained. In 1989, ERICA (Experiment in Rapidly Intensifying Cyclones over the Atlantic) employed Doppler-equipped research aircraft (Wakimoto et al. 1992, 1995; Neiman et al. 1993; Blier and Wakimoto 1995), but their deployment off the east coast of the United States implied that the storms under study were generally moving away from shore with minimal orographic influences present. These ERICA studies focused on the structure of the warm front and the bent-back warm front, but no dual-Doppler data on cold-frontal structures have been reported.

2. Data and analysis

The primary dataset implemented in this study consists of radar reflectivities and Doppler velocities measured by the tail radar of the P-3 (Jorgensen and DuGranrut 1991). The radar operates at a wavelength of 3.2 cm (X-band), has a pulse length of 150 m, a beamwidth of 1.35° in the horizontal and 1.90° in the vertical, and a Nyquist velocity of 12.9 m s⁻¹. The scanning procedure employed during COAST, referred to as the fore–aft scanning technique (FAST; Frush et al. 1986; Hildebrand 1989; Jorgensen and Smull 1993), consists of alternatively canting the radar beam fore and aft by 22.5° from a plane perpendicular to the flight track during a period of two full rotations. As the aircraft is flown along a straight flight path, the radar sweeps out a three-dimensional volume with fore and aft beams intersecting at approximately 45° angles. Thus, along a single flight leg, FAST yields two radial velocity measurements in space at time intervals of 1–5 min (depending on the range from the aircraft). The horizontal wind field is estimated from these two velocity components.

In this study, we focus on the structure and evolution of frontal rainbands first while they were far offshore

and later while they were near the coast (10–60 km offshore). Four volumes of dual-Doppler data are discussed and will be referred to by the initial times of the flight legs (0917, 0958, 1350, and 1408 UTC; all times are UTC with LST = UTC – 8 h). The 0917 and 0958 volumes sample the region of deep convection while the system was well offshore, and the 1350 and 1408 volumes provide data along the cold front when it was within 60 km of the Oregon coastline.

The National Center for Atmospheric Research (NCAR) RDSS software (Oye and Carbone 1981) was used to unfold the radial velocities (Rinehart 1991, 81, 93) and to edit the reflectivity and radial velocity fields to remove near-surface echo associated with sea clutter, beam spreading, sea spray (which reached heights of several hundreds of meters as a result of winds in excess of 20–35 m s⁻¹), echo associated with coastal orography (the 1408 volume) and second-trip echoes (Rinehart 1991, 83) associated with the sea surface.

Prior to editing the radial velocities, the component of radial velocity associated with the aircraft motion was removed. The accuracy of the resulting earth-relative radial velocity is about 1.5 m s⁻¹ (Jorgensen et al. 1983). Radial velocity errors can occur because of improper antenna pointing. These errors are often deduced from the residual motion of the ground. However, over the storm-tossed ocean, waves and sea spray constitute a nonstationary target and thus cannot be used to deduce and correct for such errors. An analysis of the surface motions over calm oceans during COAST suggested that these pointing errors were small.

The NCAR REORDER software was used to interpolate reflectivities and radial velocities from the fore and aft scans to Cartesian grids with vertical grid spacing of 500 m and horizontal grid spacing of 1.25 km at 0917, 1350, and 1408 and 1.0 km at 0958. The 1-km grid spacing at 0958 was achieved because the radar was scanning a sector to one side of the aircraft only. Although radar returns are recorded out to a range of about 80 km, only data within 40 km of the aircraft were used because of beam spreading. The radii of influence used in the interpolation were 1.5 km in the horizontal (1.25 km for 0958) and 700 m in the vertical.

During the interpolation procedure, the horizontal positions of the radar reflectivity and radial velocity data were adjusted relative to a reference time to account for the motion of clearly identifiable precipitation cores along the cold front during the approximately 10-min long flight legs. Throughout the following discussion, dual-Doppler-derived air motions will be presented relative to the mean motion of the several precipitation cores occurring within each dual-Doppler volume and will be referred to as *core-relative* air motions. Core-motion estimates were obtained during the interpolation by adjusting the advection velocity until the horizontal locations of the precipitation cores in the interpolated reflectivity fields were matched in the fore and aft scans. The core-normal component derived in this manner

compared well to the motion of the front as determined from a series of lower-fuselage radar reflectivity fields. The core-parallel component of the core motion characterized the velocity of the precipitation cores along the front. The core motion estimated for both the offshore and nearshore stages was 225° at 28 m s⁻¹. The estimated error is ±10° and 2 m s⁻¹.

The radar reflectivity field was determined by taking the maximum value of the reflectivities measured by the fore and aft scans at a given point on the Cartesian analysis grid. Precipitation fall speeds were estimated from the reflectivity values by using the empirical relationships for rain and snow given in Marks and Houze (1987). A mixed ice–rain layer was used at the 1.8-km level to approximate the fall speeds of melting particles. The height of the 0°C level was estimated from flight-level data to be 1.6 km behind the front and 2 km ahead of the front, which are within about half a vertical grid distance of the 1.8-km level. Errors in the synthesized horizontal winds associated with the fall speed corrections are expected to be small because the radar beams were nearly horizontal in these regions.

Synthesis of the gridded fore and aft radial velocities into horizontal wind fields was performed using NCAR CEDRIC (Mohr and Miller 1983). Horizontal air velocities immediately above and below the aircraft cannot be measured accurately because of the nearly vertically pointing beams. Radial velocities within a 60° wedge centered above the aircraft were removed automatically prior to editing. Interpolated radial velocities within a 40° wedge below the aircraft were removed manually within CEDRIC. Since the dual-Doppler flight track was in a region of weak horizontal velocity gradients, small gaps in the synthesized horizontal velocities above and below the aircraft were interpolated from nearby grid points. A two-step Leise filter (Leise 1981) was applied to the velocity data prior to computation of the vertical motions. This filter completely removed horizontal wavelengths less than 4Δx and retained greater than 90% of wavelengths larger than 8Δx (Δx = horizontal grid spacing = 1.0–1.25 km).

Vertical air velocities were obtained by vertical integration of the horizontal divergence using variational adjustment of the anelastic mass continuity equation subject to boundary conditions near the surface (300 m) and at echo top (O'Brien 1970). The lower boundary condition for vertical velocity was set to zero at 300 m. At echo top, the boundary condition was set to 0.25 m s⁻¹ where the reflectivity exceeded 10 dBZ (following Biggerstaff and Houze 1991) and the echo height was greater than a specified value (7.5 km at 0917 and 0958, 5 km at 1350 and 1408). Otherwise it was set to zero. Because the frontal rainband and its associated deep convection were very narrow (<15 km wide) and because of the limited horizontal grid spacing (1–1.25 km), the horizontal filtering, and the crude approximation of the boundary values at echo top, the vertical velocity fields may exhibit errors of several meters per second

within the strongest convective updrafts. Therefore, our discussion of the vertical velocity fields will generally focus more on the qualitative aspects of this field.

Further information on the distribution of horizontal and vertical air motions within the frontal zone is obtained by using the statistical analysis approach developed by Yuter and Houze (1995a,b) known as the contoured frequency by altitude diagram (CFAD). The ordinate of the CFAD is height, and the abscissa is the value of the parameter whose distribution is being plotted. Contours of the frequency of occurrence per parameter unit per unit height for the observed parameter are plotted in this coordinate system. In this manner, the CFAD succinctly summarizes the frequency distribution of a variable (including components of vector quantities) in a given radar echo volume in a single contour plot.

For CFADs of vertical velocity, it is instructive to weight the vertical velocity by the density of air and the horizontal area of the grid element to produce a CFAD of the vertical mass transport (Yuter and Houze 1995b). The contours in such a CFAD are of the vertical mass transport of air accounted for by all drafts within the vertical velocity interval w and $w + \Delta w$ and within the height interval Z and $Z + \Delta Z$. Since the contoured field is not normalized by the number of points at each level in this case, the values for the contours are dependent on the size of the echo area containing the data [section 4b(4)].

3. Observational setting and flight summary

The COAST IOP 3 flight was conducted primarily off the Oregon coast in a developing frontal system characterized by regions of deep convection along the cold front during its offshore stage and a more typically observed NCFR structure during the nearshore stage. Figure 1 shows infrared satellite imagery for the IOP3 storm. The images at 0900 and 1500 UTC (Figs. 1c,d) correspond approximately to the times of the offshore (0917 and 0958) and nearshore (1350 and 1408) dual-Doppler volumes, respectively. Corresponding National Centers for Environmental Prediction (NCEP, formerly National Meteorological Center) surface and 500-mb analyses are shown in Figs. 2 and 3.

At 0000 (Fig. 1a), the developing frontal system was characterized by a north-south-oriented, comma-shaped cloud band near 40° – 45° N, 139° W (this cloud band is hereafter referred to as the comma cloud). The comma cloud lacked a well-defined warm-frontal signature in the satellite image. The sea level pressure and temperature fields (Fig. 2a) depict the IOP 3 system as a developing frontal wave. A dissipating frontal system lay ahead of the IOP 3 storm near 130° W. At upper levels (Fig. 3a), the comma cloud was situated just ahead of a 500-mb trough with a strong west-northwesterly jet to the west and diffluent southwesterly flow to the east.

By 0600 (Fig. 1b), the comma cloud had progressed rapidly eastward to 132.5° W. The P-3 departed Boeing

Field in Seattle at 0630 and headed westward toward the frontal system. By 0900, the P-3 was near the southern end of the comma cloud (42° N, 129° W in Fig. 1c). The cloud shield had begun to wrap around the low center. Figures 4a,b show 3.5-min composites of radar reflectivity from the lower-fuselage radar at the times of the dual-Doppler syntheses. The P-3 was flying along a portion of the NCFR that was characterized by intense deep convection and was producing frequent lightning. Reflectivities decreased north and south of the dual-Doppler boxes because of beam spreading, attenuation, and the slight vertical tilt of the radar above horizontal, which caused the radar to sample increasingly higher elevations with distance from the aircraft. North of the dual-Doppler boxes, the convection was apparently more disorganized, whereas to the south, convection occurred sporadically along a generally shallower but intense portion of the NCFR.

Surface and upper-level synoptic conditions at 1200 UTC 8 December, approximately 2 h prior to the nearshore dual-Doppler volumes, are shown in Figs. 2b and 3b. The surface isotherm pattern shows a well-developed frontal wave. At 500 mb, the trough axis had sharpened and progressed to 130° – 135° W and the height contours ahead of the trough implied a stronger southerly geostrophic wind component just west of the coastline compared to 0000 UTC. Comparison of the meridional component of velocity in the offshore and nearshore dual-Doppler volumes confirmed this general increase in the southerly flow as the system approached the coast.

By 1300, little lightning was observed and the intense radar echoes along the NCFR were much shallower with high-reflectivity cores (>25 dBZ) generally not extending above 5 km. The satellite image for 1500 (Fig. 1d) shows a well-developed cyclone with the cloud shield wrapping around the low center well to the west. The NCFR (Figs. 4c,d) was oriented approximately parallel to the coastline and exhibited a horizontal reflectivity substructure similar to that described by James and Browning (1979), Hobbs and Biswas (1979), and Hobbs and Persson (1982) for NCFRs. The front first made landfall near Cape Blanco (42.8° N, 124.5° W) on the southern Oregon coast at 1430 UTC. Two dual-Doppler volumes near this time (Figs. 4c,d) captured this portion of the front just prior to landfall.

4. Precipitation and kinematic structure

a. Offshore structure of the NCFR and associated deep convection

The frontal rainband was first detected on the lower-fuselage radar at about 0800 as the aircraft approached from the east. Frequent lightning was observed in the deep convection along the front. Between 0913 and 0945 (see Fig. 4a), the P-3 flew at 1600 m parallel to the front on its eastern (warmer) side. A 10-min flight leg beginning at 0917 provided the data for the first

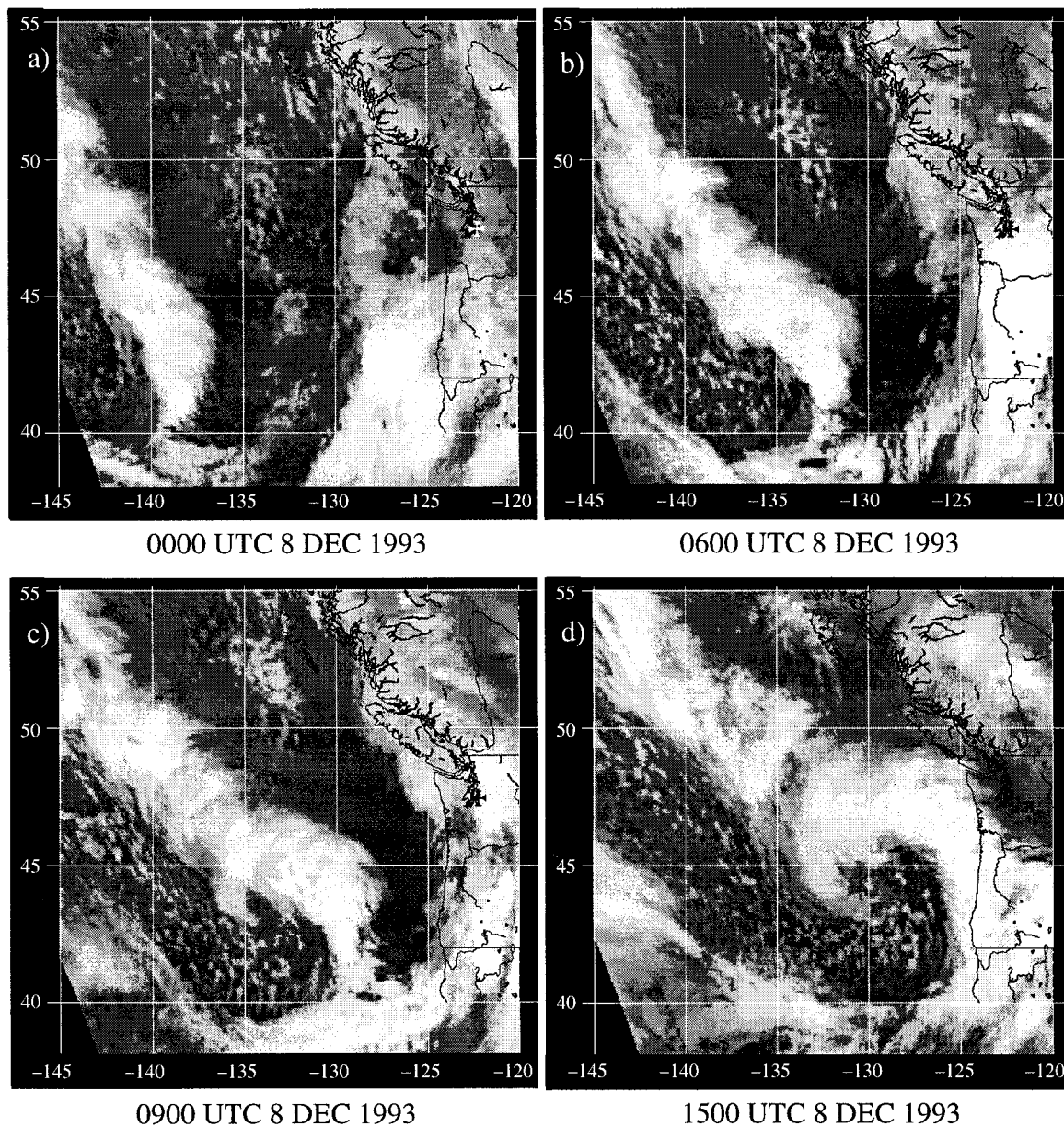


FIG. 1. Infrared satellite images for 8 December 1993. The location of Boeing Field in Seattle, Washington, is indicated by the cross.

dual-Doppler synthesis. The dual-Doppler domain is indicated by the box in Fig. 4a. The P-3 was located immediately ahead of the intense convection, and the tail radar scanned the regions on both sides of the aircraft. At 0950, the P-3 crossed the front and flew parallel to the front on its western (cold) side (Fig. 4b). Because of the lack of precipitation on the cold side of the intense rainband, the tail radar scanned a sector to one side of the aircraft only. A second dual-Doppler synthesis was performed for a 7-min flight leg beginning at 1002 (Fig. 4b). Comparison of Figs. 4a and 4b suggests that the intense convection observed at 0922 had spread farther south along the NCFR by 1002. The maximum reflectivities exceeded 50 dBZ at 1002.

The potential for deep convection on this day is indicated by a sounding (Fig. 5) constructed from flight-level data collected well ahead of the front near 43°N , 125°W (Fig. 2b). A surface parcel forced upward by the front would reach its level of free convection (LFC) near 840 mb (1.5 km) and would remain positively buoyant up through 500 mb, where its temperature excess would be 2 K. Since the frontal density current was often deeper than 2 km, surface parcels were likely forced above the LFC along portions of the front. The following subsections examine the kinematic and precipitation structure of the convection apparently produced by the lifting of this potentially unstable air by the density current associated with the cold front.

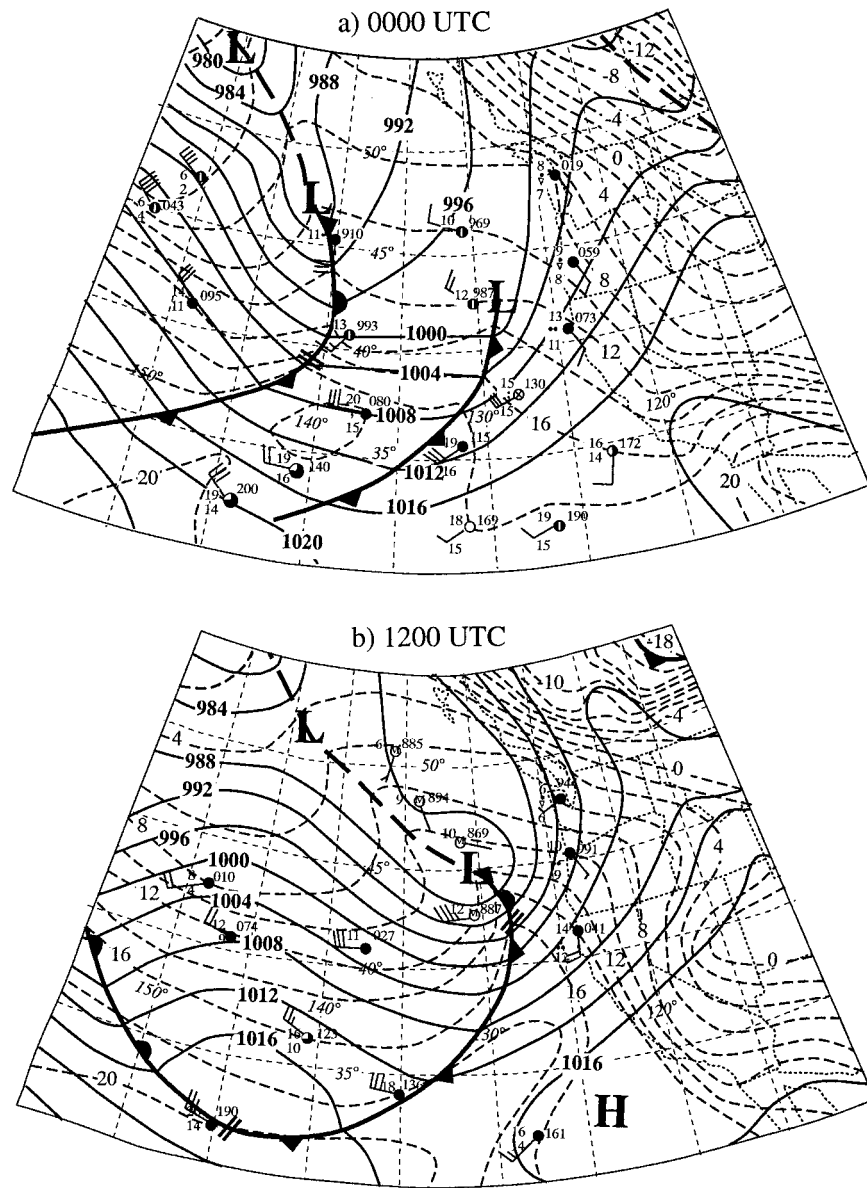


FIG. 2. Sea level pressure and temperature analyses for 8 December 1993. The solid lines are isobars at 4-mb intervals and the dashed lines are isotherms at 2°C intervals. Stations depict temperature (°C), dewpoint temperature, and pressure to the upper left, lower left, and upper right of the station circle. Full wind barbs correspond to 5 m s⁻¹, half-barbs to 2.5 m s⁻¹.

1) KINEMATIC AND PRECIPITATION STRUCTURE AT 0917

The 0917 dual-Doppler analysis at 800 m is shown in Fig. 6. The zonal (X) component is denoted as U and the meridional (Y) component as V . The U and V components are also generally referred to as the across- and along-front components, respectively. Terms such as “behind, ahead, rear, and front” refer to a reference frame oriented normal to the NCFR with the rear portion of the system located toward the west.

The radar reflectivity field (Fig. 6a) depicts an intense,

relatively continuous convective line between $Y = -75$ and -128 km that was aligned with the front. This convective band is designated CB in Fig. 6a and is referred to hereafter as the convective band to distinguish it from other sections of the NCFR that were generally much shallower and characterized by weaker vertical velocities. The precipitation along the front was significantly less intense to the north ($Y > -75$ km) of the convective band (see also Fig. 4a). To the south ($Y < -128$ km), the reflectivities showed a somewhat broken pattern resembling structures more typical of NCFRs. Three weaker bands (labeled B1, B2, and B3 in Fig.

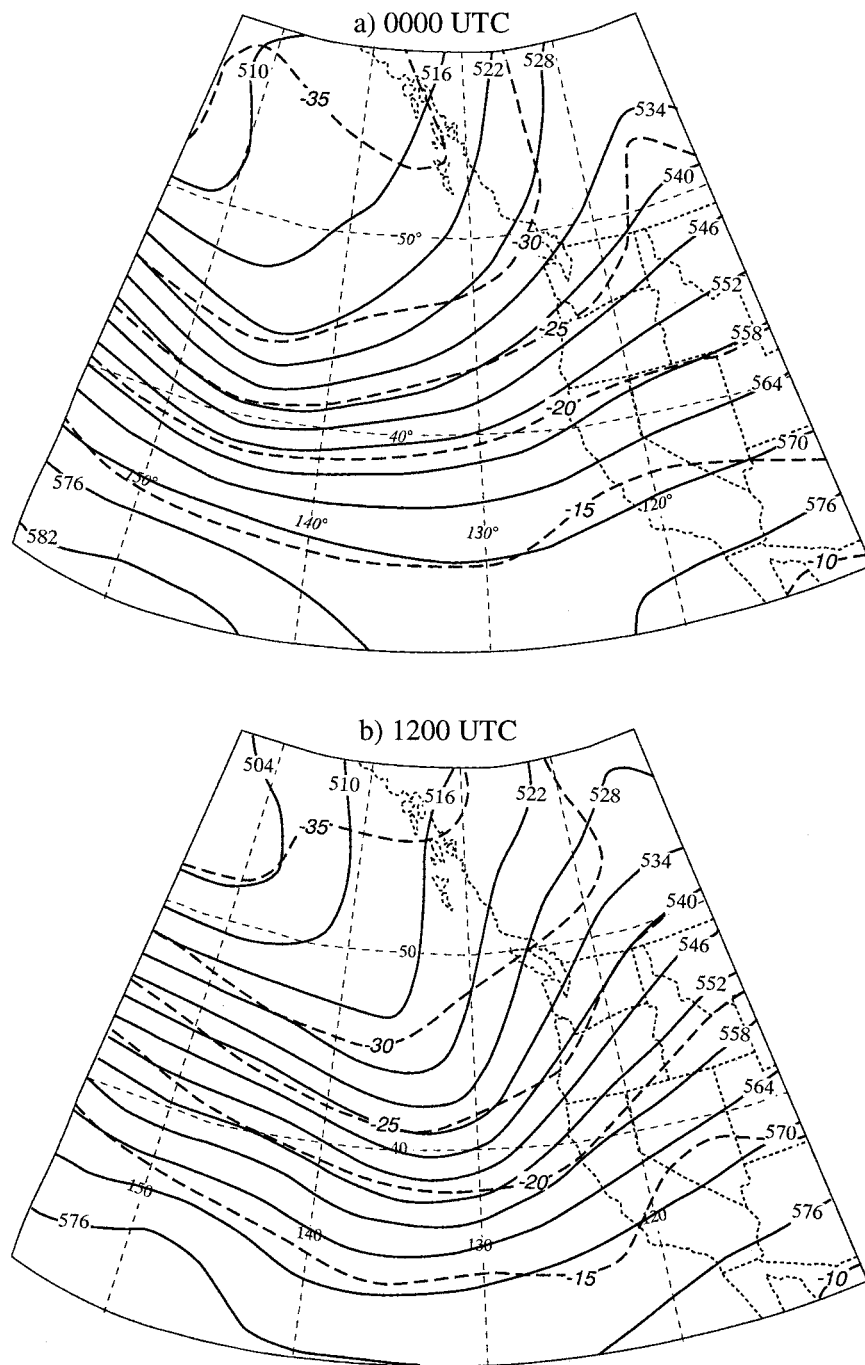


FIG. 3. Geopotential height and temperature analyses at 500 mb for 8 December 1993. Geopotential heights (solid lines) are contoured at 60-m intervals. Temperature (dashed lines) are contoured at 5°C intervals.

6c) were oriented roughly perpendicular to and positioned ahead of the convective portion of the NCFR and were spaced approximately 10–15 km apart. Following Houze et al. (1976), these bands are referred to as wavelike rainbands. The wavelike bands extended eastward into a wide region of stratiform precipitation, which was much weaker or absent to the south. Raw reflectivity

data from the tail radar indicated that B2 was composed of an ensemble of shallow, very narrow, and intense convective elements rather than intense stratiform precipitation. Rainband B3 was entirely stratiform, whereas band B1 was stratiform with embedded shallow convection.

Houze et al. (1976, see their Fig. 3) presented a sche-

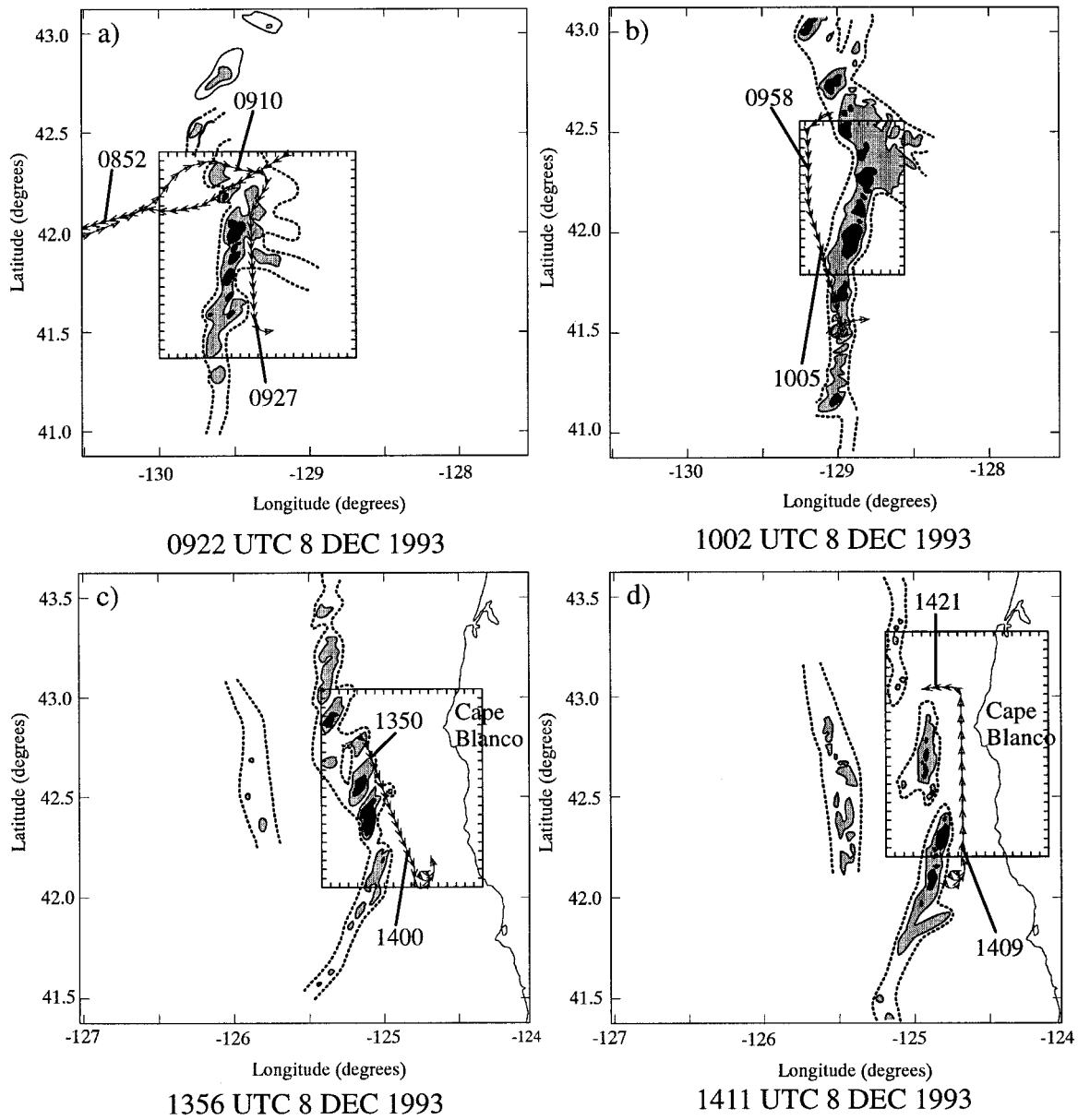


FIG. 4. Radar reflectivity composites from the lower-fuselage radar. Contour lines are drawn at 27.5, 35, and 42.5 dBZ. Reflectivities greater than 42.5 dBZ are darkly shaded and reflectivities between 35 and 42.5 dBZ are lightly shaded. The 27.5-dBZ contour lines are dashed where they were subjectively distinguished from the surrounding echo from the ocean surface. The coast is indicated by the thin solid line on the right side in panels (c) and (d). Portions of the flight track corresponding to the times of the dual-Doppler legs are indicated by the solid lines with arrows, which indicate aircraft positions at 1-min intervals. Regions of dual-Doppler coverage are indicated by the boxes with tick marks every 5 km.

matic analysis of rainbands documented in a cyclone approaching the Washington coast on 27–28 November 1973. Along a segment of the cold front immediately to the south of the triple point (the juncture between the cold, warm, and occluded fronts), their analysis showed wavelike rainbands oriented at large angles with respect to the NCFR, very similar to the pattern seen in Fig. 6. In the 27–28 November 1973 storm, the wavelike rainbands were also apparent in a wide region of light rainfall that trailed the NCFR and were observed to cross

the NCFR in the region south of the triple point. It is possible that the wavelike rainbands observed in the IOP 3 storm are similar to those described in Houze et al. (1976), except that they are not seen in the region trailing the NCFR because of the lack of precipitation there. Neiman et al. (1993) found similar transverse bands ahead of an intensely convective portion of a cold front in the 4–5 January 1989 cyclone observed during ER-ICA. The *U* velocity field (Fig. 6b) indicates strong con-

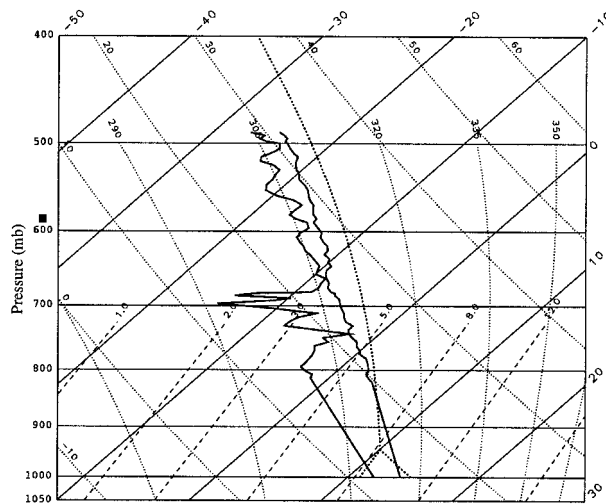


FIG. 5. Skew T - $\log p$ diagram depicting the thermodynamic conditions well ahead of the cold front. The profiles were obtained from flight-level temperature and dewpoint temperature between 1244 and 1255 UTC 8 December 1993 near 43°N , 125°W . Profiles below 820 mb have been linearly interpolated from nearby surface values. A representative moist adiabat is indicated by the thin dotted line.

vergence along the length of the cold front. Westerly core-relative velocities in the postfrontal air, up to 8 m s^{-1} , were maximum in the region $Y < -110\text{ km}$, primarily behind the southern portion of the convective band. Core-relative easterly flow in excess of 7.5 m s^{-1} occurred ahead of precipitation cores PC1 and PC2. The inflow was weakest along the southern edge of rainband B1 but rapidly increased from 8 to 13 m s^{-1} near band B2. The V velocity field (Fig. 6c) was characterized by northerly core-relative flow behind the front and southerly flow ahead of the front. There was a local minimum of the southerly flow to the south of band B1 and a local maximum between bands B1 and B2.

Doppler-derived vertical velocities w at 1.8 km and 6.3 km are shown in Fig. 7. At 1.8 km (Fig. 7a), the vertical velocities indicate a continuous line of updraft associated with the front and several updraft cores along the front. Each core had a comparable amplitude of about 6 m s^{-1} and was generally associated with a core of higher reflectivity. Convective downdrafts were located behind the northern end and the central portion of the convective band. The updrafts in the convective band extended vertically above the 6.3-km level (Fig. 7b), with the strongest drafts located at the northern and southern ends of the convective band. The low-level updraft associated with precipitation core PC2 was very weak at the 6.3-km level, indicative of the shallower structure south of the convective band at this time.

Vector winds at 1.8 km (Fig. 7a) indicate the strongest westerly flow behind the northern and central portions of the convective band ($Y = -80$ to -115 km), whereas at 800 m (Fig. 6b), the maximum westerlies lay generally behind and to the south of the southern portion of the convective band. At 800 m, a narrow tongue of

stronger westerlies extended toward the central part of the convective band ($Y = -108$ to -115 km) and a second core of strong westerlies was near the northern end of the convective band ($Y = -88\text{ km}$). The vertical velocities and vector winds in Fig. 7a suggest that the stronger 800-m westerlies between $Y = -108$ to -115 km and near $Y = -88\text{ km}$ were where the elevated (1.8 km) westerly flow was transported downward toward the surface by the convective downdrafts. For example, the core of strong westerlies at the northern end of the convective band was associated with a convective downdraft (Fig. 7a) emanating from the intense convection near the intersection of the front and band B2. At 6.3 km, the vector winds indicate strong rearward outflow behind the northern end of the convective band and little or no rearward flow to the south.

Cross-frontal thermodynamic and kinematic characteristics are indicated by flight-level data (Fig. 8) at 1600 m during a westbound pass across the front just to the north of the convective band (near $Y \approx -60\text{ km}$ in Fig. 6 and near 42°N , 130° – 135°W in Fig. 4a) for the 13-min period from 0844 to 0857. The flight-level pressures have been adjusted to the 1600-m level using flight-level temperatures to correct hydrostatically for slight departures in altitude. The left side of the diagram corresponds to the warm side of the front. Between 0846 and 0849, the wind direction veered from about 210° to 250° . A prefrontal jet reached a peak magnitude of 45 m s^{-1} (indicated by the vertical line labeled T1 in Fig. 8) immediately prior to a sharp directional wind veer and a rapid jump in the temperature and potential temperature and just following a pressure minimum. The lowest pressure (816 mb at T2) coincided with the maximum potential temperature and a relative minimum of wind speed and wind direction just after 0848. Vertical velocities showed an 11 m s^{-1} updraft followed by a 7 m s^{-1} downdraft and then more quiescent conditions. The rear edge of the frontal rainband was encountered near T3, where the wind direction changed rapidly from 215° to 250° , the equivalent potential temperature dropped rapidly by 8 K, and the vapor mixing ratio decreased 2 – 3 g kg^{-1} (not shown). The temperature and potential temperature declined more slowly behind the front compared to the equivalent potential temperature, indicative of marked drying behind the frontal rainband.

The vertical cross-frontal structure of the northern portion of the convective band, along the line $Y = -90\text{ km}$ in Fig. 6, where band B2 intersected the front, is shown in Fig. 9. High reflectivities ($>25\text{ dBZ}$) associated with the convective band ($X = -402$ to -410 km) extended upward to 9 km. A secondary reflectivity maximum ($X = -393$ to -401 km) was associated with band B2. Stratiform precipitation lay primarily ahead of the convective band. Behind the convective band, ice particles detrained by the divergent outflow aloft did not fall below about 3–4 km, apparently as a result of sublimation in dry westerly flow entering the rear of the system (Fig. 9c).

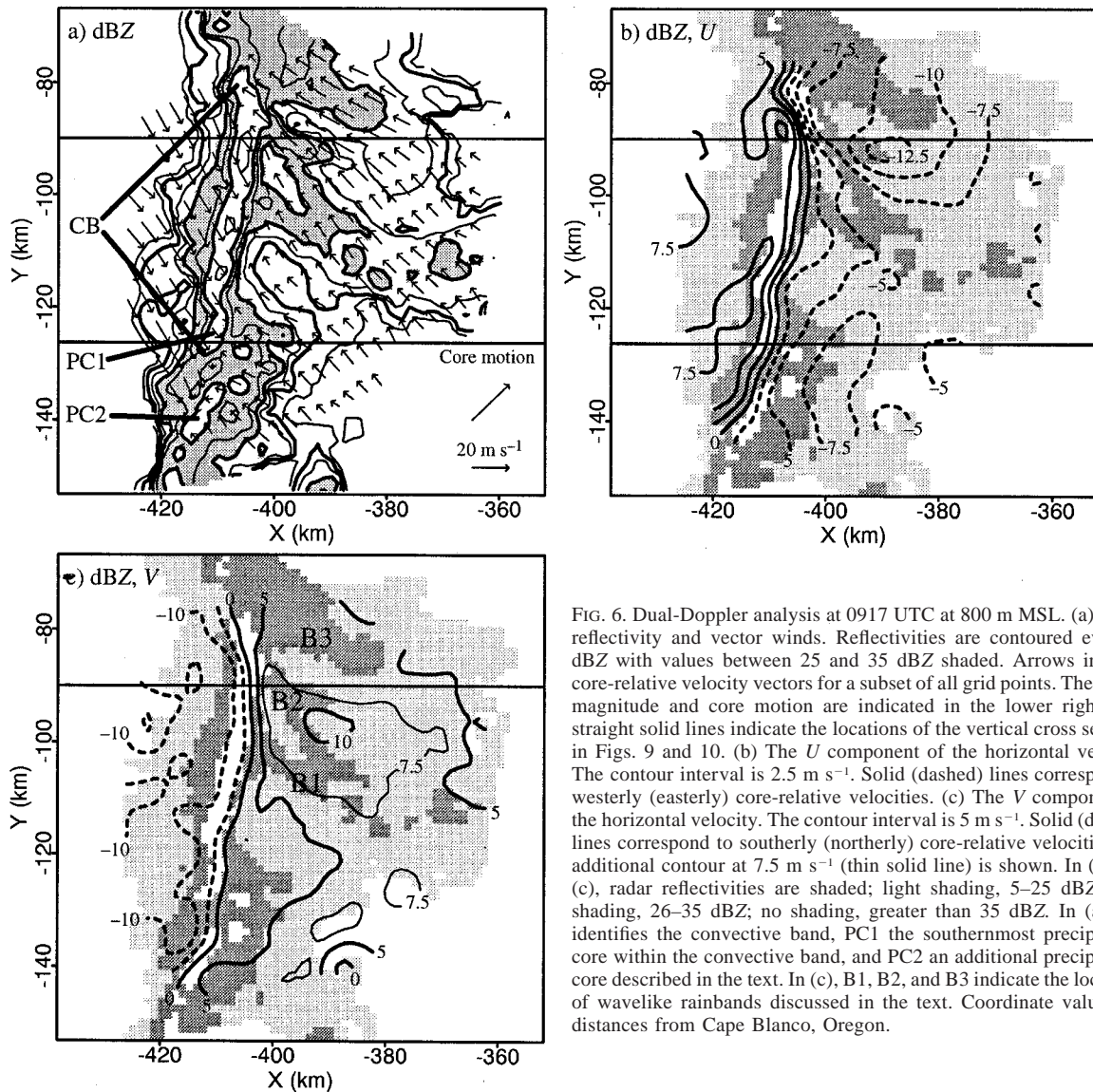


FIG. 6. Dual-Doppler analysis at 0917 UTC at 800 m MSL. (a) Radar reflectivity and vector winds. Reflectivities are contoured every 5 dBZ with values between 25 and 35 dBZ shaded. Arrows indicate core-relative velocity vectors for a subset of all grid points. The vector magnitude and core motion are indicated in the lower right. The straight solid lines indicate the locations of the vertical cross sections in Figs. 9 and 10. (b) The U component of the horizontal velocity. The contour interval is 2.5 m s⁻¹. Solid (dashed) lines correspond to westerly (easterly) core-relative velocities. (c) The V component of the horizontal velocity. The contour interval is 5 m s⁻¹. Solid (dashed) lines correspond to southerly (northerly) core-relative velocities. An additional contour at 7.5 m s⁻¹ (thin solid line) is shown. In (b) and (c), radar reflectivities are shaded; light shading, 5–25 dBZ; dark shading, 26–35 dBZ; no shading, greater than 35 dBZ. In (a), CB identifies the convective band, PC1 the southernmost precipitation core within the convective band, and PC2 an additional precipitation core described in the text. In (c), B1, B2, and B3 indicate the locations of wavelike rainbands discussed in the text. Coordinate values are distances from Cape Blanco, Oregon.

The vertical velocity field (Fig. 9b) exemplifies the complicated vertical motion structure within the convective band in the region where bands B1 and B2 intersected the front ($Y = -80$ to -105 km, Fig. 6c). Near $X = -404$ km and below 4 km, there was an updraft core with $w > 6$ m s⁻¹ associated with the leading edge of the front. A stronger updraft core ($w > 11$ m s⁻¹) was centered near $X = -410$ km and heights of 6–7 km and suggests a rearward tilting, organized multicellular structure of the convection along the front. A convective downdraft located below this updraft was associated with the local downward penetration of the westerly flow seen in Fig. 6b. An additional elevated strong updraft ($w > 6$ m s⁻¹) was collocated with band B2 near $X = -398$ km.

The cross section of across-front flow (U) through

the convective band shows a nearly 6-km-deep layer of westerly flow behind the convective line (Fig. 9c) with maximum velocities just above the melting level. In contrast to the deep westerly flow behind the convective band, the post-frontal westerly flow behind PC1 (Fig. 10b) and PC2 (not shown) was relatively shallow (only up to 3 km). It is unclear whether the deeper layer of westerly postfrontal flow behind the northern portion of the convective band was present before the onset of the deep convection, thereby acting to force it, or if it developed in response to the convection. Strong westerly flow also occurred at upper levels ahead of the line and was associated with strong larger-scale westerly flow as well as divergent outflow from the convection. This strong westerly outflow aloft carried significant amounts of precipitation generated within the convective updrafts

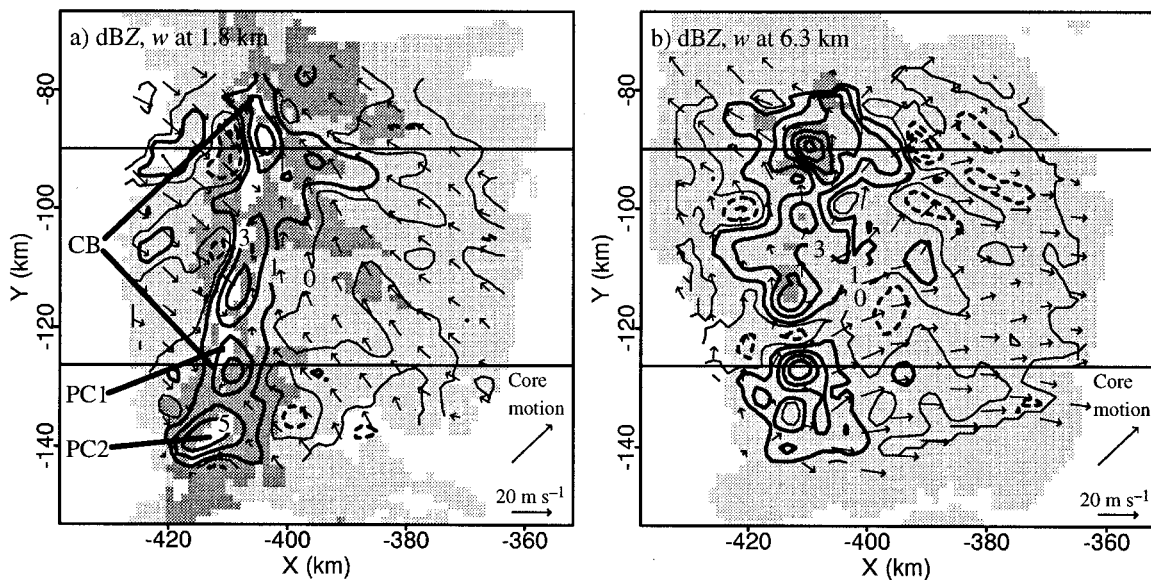


FIG. 7. Radar reflectivity, core-relative velocity vectors, and vertical velocity at (a) 1.8 km and (b) 6.3 km MSL at 0917 UTC. Radar reflectivities are shaded; light shading, 5–25 dBZ; dark shading, 26–35 dBZ; no shading, greater than 35 dBZ. Arrows indicate core-relative velocity vectors for a subset of all grid points. The vector magnitude and core motion are indicated in the lower right. Contours of upward motion (solid lines) are drawn at 2 m s^{-1} intervals beginning at 1 m s^{-1} . Contours of downward motion (dashed) are drawn at 1 m s^{-1} intervals beginning at -1 m s^{-1} . The thin solid contour corresponds to 0 m s^{-1} . In (a), CB identifies the convective band, PC1 the southernmost precipitation core within the convective band, and PC2 an additional precipitation core described in the text. The straight solid lines indicate the locations of the vertical cross sections in Figs. 9b and 10b.

into the region ahead of the convective line, where it contributed to the stratiform precipitation. Core-relative easterly flow occurred at lower levels ahead of the line and at upper levels behind the line, and was generally weakest within the convective updrafts. Along a small portion of the convective band ($Y \approx -95$ to -105 km , Fig. 6), a weak relative maximum of easterly flow coincided with the updraft at midlevels.

The deep convection along the NCFR shows qualities similar to midlatitude squall lines in its across-front flow. Across-line horizontal flows in squall lines (see Fig. 1 of Houze et al. 1989) are often characterized by ascending front-to-rear and descending rear-to-front flows (e.g., Smull and Houze 1985, 1987; Houze et al. 1989). The rear-to-front flow often forms a jetlike structure near the melting level and then descends to the surface in the convective region. The front-to-rear flow often has maximum amplitude in the convective updraft. In the NCFR, core-relative rear-to-front flow occurred behind the convective band and was maximized near the melting level. Unlike some midlatitude squall lines, however, the front-to-rear flow was generally weak in the convective updraft.

The along-front flow (V) is shown in Fig. 9d. A narrow core of stronger southerly flow was at $X = -400 \text{ km}$ and a height of 2 km. This feature was apparent ahead of the northern portion of the convective band in association with the stronger southerly flow adjacent to band B2 (Fig. 6c). Northerly core-relative flow occurred behind the front and, at this location, a tongue of north-

erly and weak southerly momentum air extended upward to 8 km. This feature was present at 0917 only in association with the intense convective updraft at the northern end of the convective band (Fig. 7; similar flow structure was also seen within intense portions of the convective band at 0958, not shown), and indicates that, in addition to the warm sector air, air within the frontal zone was occasionally rising in connection with the strong convective circulations.

Across precipitation core PC1, located at the southern end of the convective band (Fig. 6a), the updraft was deep (Fig. 10a), but the region of high reflectivity above 4 km was not as deep or intense as across the northern portion of the convective band (Fig. 9). While the flow structure ahead of the front was comparable to the northern cross section, the westerly flow behind the front was much shallower. The low-level easterly flow rose above the front, but did not penetrate into upper levels. Easterly flow aloft was very weak compared to the northern portion of the convective band. The flow structure across PC1 was very similar to that seen during the nearshore stage of the storm (section 4b).

2) KINEMATIC CHARACTERISTICS REVEALED BY CFADS

Figures 11a,b present the CFADs for the U and V components of the core-relative horizontal velocities at 0917. Above 3 km, the distribution of U is relatively narrow, with U increasing with height (Fig. 11a). This

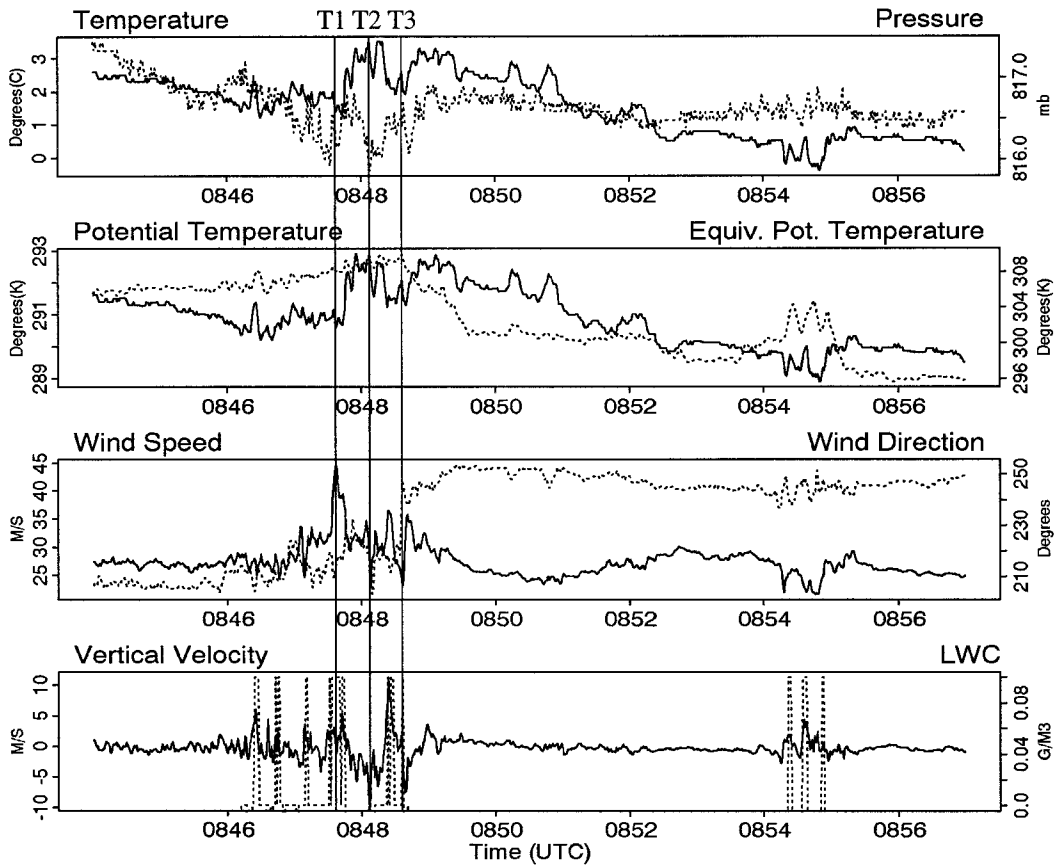


FIG. 8. Flight-level data for the period 0844 to 0857 UTC at 1600 m MSL for a pass across the cold front. The parameter indicated above the upper left (right) of each panel corresponds to the solid (dotted) line. The flight-level pressure has been adjusted to the 1600-m level using flight-level temperature to account for small departures of the flight track from this level. LWC refers to liquid water content. Vertical lines correspond to specific times discussed in the text.

shear is indicative of the presence of deep baroclinity in the north–south direction in the large-scale environment (Figs. 2 and 3). The distribution at uppermost levels is broadened as a result of the local influence of strongly divergent upper-tropospheric outflow emanating from the deep convection. Below 3 km, the distribution is bimodal, with distinct velocity modes representing flow within the pre- and postfrontal air masses. The postfrontal westerly flow ($U > 0 \text{ m s}^{-1}$ below 3 km) increased with height. Combined with the deep layer of low-level inflow ($U < 0 \text{ m s}^{-1}$), this structure is indicative of the deep layer of convergence associated with the convection and the elevated postfrontal westerly jet (Fig. 9c). The along-front velocities (Fig. 11b) show a relatively wide distribution above 3 km, which changed only slightly with height. Below 3 km, a bimodal distribution occurred. The width of the gap between the two modes is effectively a measure of the mean relative vorticity associated with the front. A shear-zone width of 8 km (Fig. 6b) suggests a mean vorticity of about $22f$, where f is the Coriolis parameter. Maximum gridpoint values of vorticity (not shown)

were near $65f$ in association with the intense convection at the north end of the convective band.

3) KINEMATIC AND PRECIPITATION STRUCTURE AT 0958

The P-3 resampled the frontal band approximately 41 min later beginning at 0958. The lower-fuselage radar reflectivity pattern at 1002 and the location of the 0958 dual-Doppler box are shown in Fig. 4b. The lower-fuselage reflectivity pattern indicates an intensification and slight widening of the frontal rainband since the previous dual-Doppler time (Fig. 4a). Echoes exceeding 42 dBZ increased in area and echoes greater than 35 dBZ extended farther south along the front. The portion of the frontal rainband within the 0958 dual-Doppler box is approximately the same as that in the 0917 dual-Doppler box, if one accounts for the motion of the precipitation cores along the front.

The 800-m reflectivity and core-relative vector winds for the 0958 dual-Doppler volume are displayed in Fig. 12a and fields from a representative vertical cross sec-

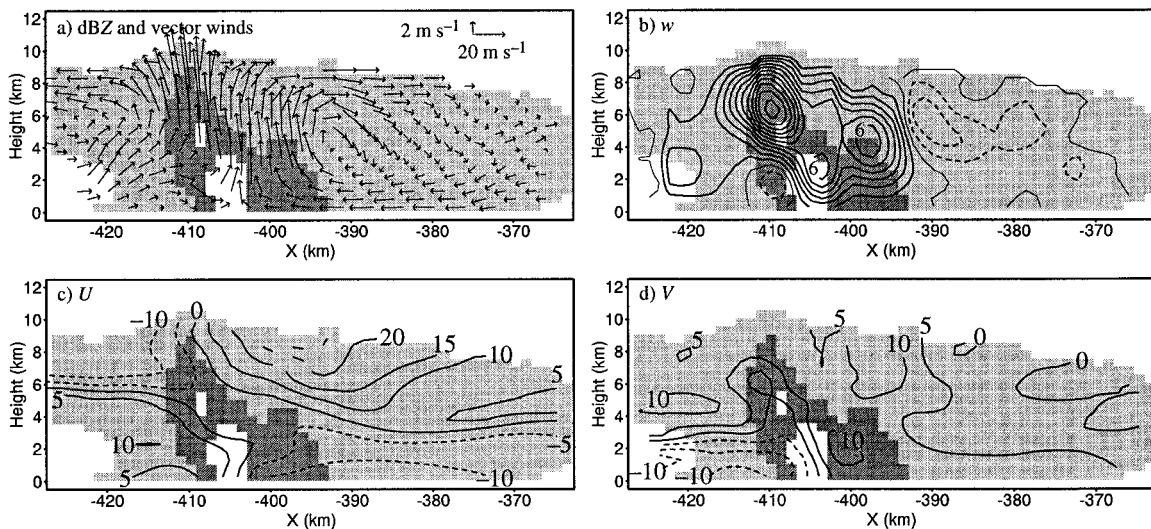


FIG. 9. Vertical cross sections at $Y = -90$ km at 0917 UTC (Fig. 6). Radar reflectivity is shaded; light shading, 5–25 dBZ; dark shading, 26–35 dBZ; no shading, greater than 35 dBZ. (a) Core-relative circulation vectors. The magnitudes of the horizontal and vertical components are indicated in the upper-right corner. (b) Vertical velocity, contoured at 1 m s^{-1} intervals. Solid (dashed) lines indicate upward (downward) vertical velocities. The thin solid line is the 0 m s^{-1} contour. (c) The U and (d) V components of the horizontal core-relative velocity, contoured at 5 m s^{-1} intervals. Solid (dashed) lines correspond to westerly (easterly) flow in (c) and to southerly (northerly) flow in (d).

tion are shown in Figs. 12b and 12c. This cross section (at $Y = -76$ km) is located about 14 km northward of the cross section in Fig. 9 ($Y = -90$ km) in a front-relative reference frame, which was moving eastward at 20 m s^{-1} . Since the precipitation cores at the front

moved at a speed of about 20 m s^{-1} along the front, the cross section cuts roughly across the portion of the rainband that evolved from PC1 in the 0917 dual-Doppler volume.

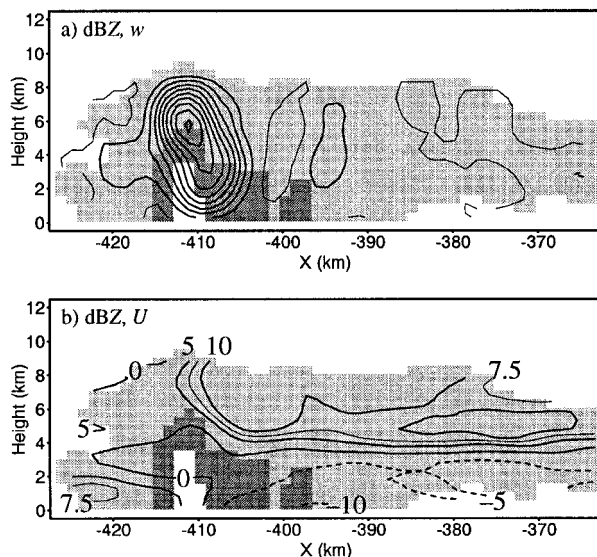


FIG. 10. Vertical cross sections at $Y = -126$ km at 0917 UTC (Fig. 6). Radar reflectivity is shaded; light shading, 5–25 dBZ; dark shading, 26–35 dBZ; no shading, greater than 35 dBZ. (a) Vertical velocity contoured at 1 m s^{-1} intervals. Solid (dashed) lines indicate upward (downward) vertical velocities. The thin solid line is the 0 m s^{-1} contour. (b) The U component of the horizontal core-relative velocity contoured at 5 m s^{-1} intervals. An additional contour is drawn at 7.5 m s^{-1} (thin solid line). Solid (dashed) lines correspond to westerly (easterly) flow.

The vertical velocity field in Fig. 12b shows an intense convective updraft at the leading edge of the frontal band ($X = -354$ km) that tilted significantly to the west with height. A second strong updraft was located farther rearward at upper levels. Compared with the reflectivity structure along the convective band at 0917 (Fig. 9), the region of reflectivities exceeding 35 dBZ approximately doubled in width and extended vertically to near 7 km. At 0958, the region of reflectivities greater than 25 dBZ associated with PC1 extended well to the rear of the front at upper levels, whereas at 0917 (Fig. 10) reflectivities at upper levels behind the precipitation core were weak.

The across-front velocity field (Fig. 12c) shows a midlevel core of strong front-to-rear (easterly) velocities within the convective updraft in the 3–6-km layer, in contrast with the weak midlevel easterly flow at 0917 (Fig. 9c). Postfrontal westerly velocities were maximum near the melting level and a weak secondary core of westerlies (up to 2.5 m s^{-1}) was just above this westerly jet near the back edge of the rainband. The westerly flow was somewhat weaker than that shown in the northern vertical cross section at 0917 (Fig. 9c), but was stronger and deeper than that found behind PC1 at that time (Fig. 10b). This raises the question of whether the deep postfrontal westerly flow behind PC1 at 0958 developed in response to the intensification of the precipitation core after 0917, in a manner similar to rear-inflow development in squall lines (Weisman 1992), or if PC1

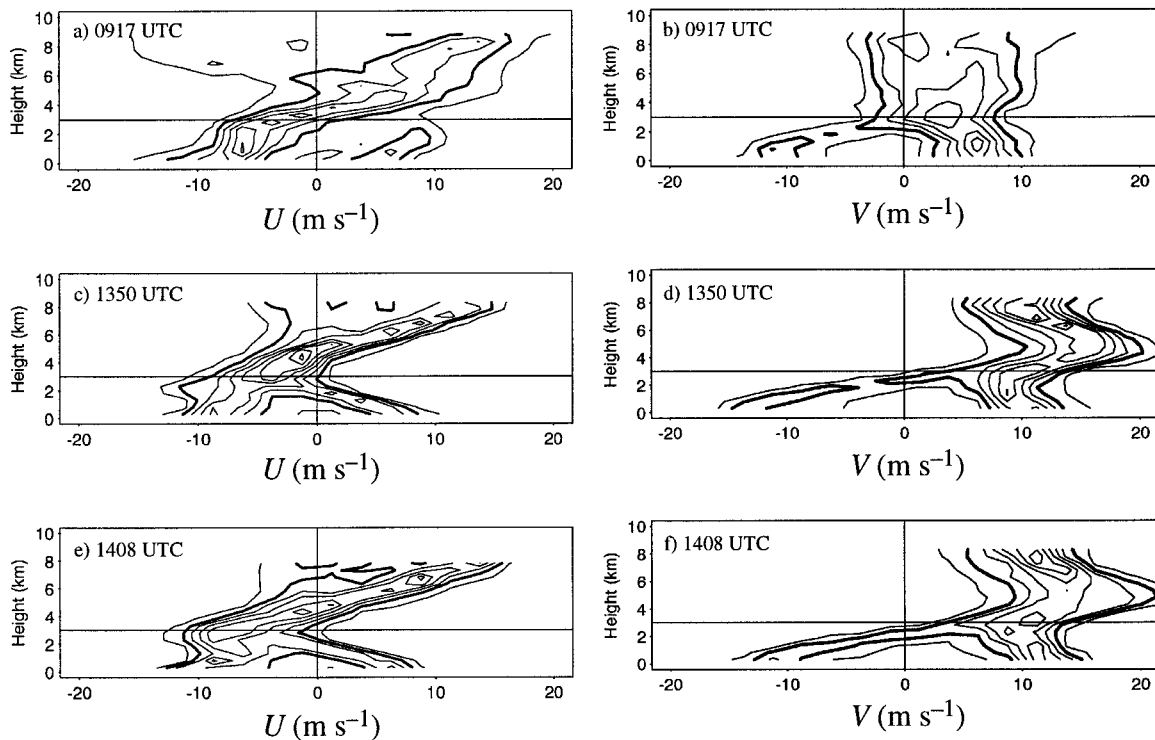


FIG. 11. CFADs of U and V , the X and Y components of the horizontal core-relative velocities. The bin size is 2.5 m s^{-1} and the vertical grid increment is 500 m . The frequencies are normalized by the number of points at each level. The contour level is $5\% (\text{m s}^{-1})^{-1} \text{ km}^{-1}$, and the bold contour represents $7.5\% (\text{m s}^{-1})^{-1} \text{ km}^{-1}$. The horizontal and vertical lines mark the 3-km level and the 0 m s^{-1} velocity value, respectively.

intensified as it moved along the front into a region characterized by a deep postfrontal westerly flow branch associated with the synoptic-scale cyclone previously observed behind the northern portion of the convective band at 0917. This issue cannot be resolved in this study but could be addressed in future observational or numerical experiments.

b. Nearshore structure of the NCFR

By 1400, the cold front was rapidly approaching the Oregon coastline and would soon make landfall at Cape Blanco (Fig. 1d shows the frontal cloud position shortly after landfall; Figs. 4c,d show the location of the NCFR relative to Cape Blanco). The lower-fuselage reflectivity pattern at 1356 (Fig. 4c) shows the front approximately 50 km offshore near the southern end of the dual-Doppler box and as much as 100 km offshore to the north and south. The reflectivity and velocity data from the tail radar did not extend to the coast at this time. At 1411 (Fig. 4d), the front was within about 30 km of the coast (20 km by the end of the dual-Doppler flight leg at 1418). Stratiform precipitation extended over the terrain near Cape Blanco. The nearshore dual-Doppler volumes for 1350 and 1408 provide detailed information on the structure and evolution of the NCFR and suggest possible orographic influences on the rainband.

1) KINEMATIC AND PRECIPITATION STRUCTURES

Figures 13 and 14 show the 800-m reflectivity and core-relative velocity fields at 1350 and 1408, respectively, as the front approached to within 20 km of the coast. The reflectivity patterns depict a NCFR structure similar to those reported in Hobbs and Biswas (1979), James and Browning (1979), and Hobbs and Persson (1982) with precipitation cores oriented at an angle to the synoptic-scale front. The precipitation cores in Figs. 13c and 14c were rotated anticyclonically approximately 15° relative to the mean orientation of the wind-shift zone, somewhat less than the $30^\circ\text{--}40^\circ$ reported by Hobbs and Biswas (1979) and Hobbs and Persson (1982).

At 1350, three precipitation cores (labeled PC3, PC4, and PC5 in Fig. 13a) had peak reflectivities exceeding 45 dBZ . The precipitation cores were much shallower than the convective band observed offshore but were similar in depth to PC2 at 0917. However, low-level reflectivities in the precipitation cores were of equal or greater magnitude than those in the convective band. By 1408, PC4 rapidly dissipated while PC3 and PC5 remained intense. An important question is what processes maintained PC3 and PC5 while simultaneously weakening PC4?

At 1350, the across- and along-front velocity fields (Figs. 13b and 13c, respectively) were quasi-two-di-

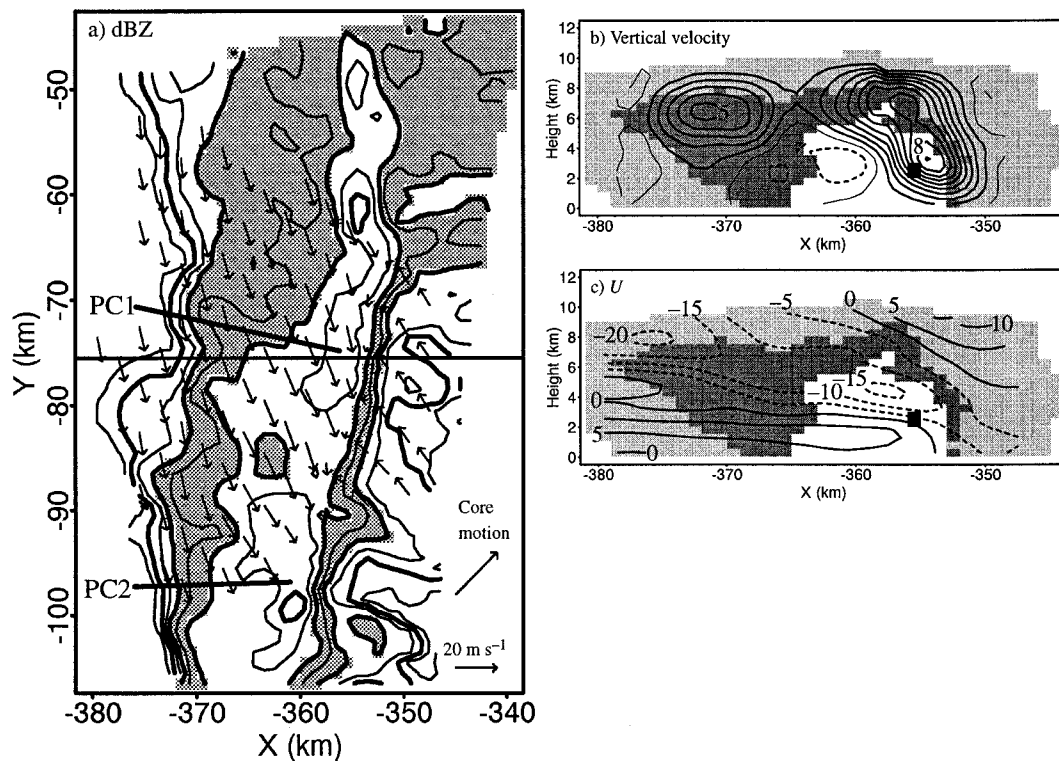


FIG. 12. Dual-Doppler analysis at 0958 UTC at 800 m MSL. (a) Radar reflectivity and vector winds. Reflectivities are contoured every 5 dBZ, and values between 25 and 35 dBZ are shaded. Arrows indicate core-relative velocity vectors for a subset of all grid points. The vector magnitude and core motion are indicated in the lower right. The straight solid line indicates the location of the vertical cross sections in (b) and (c). (b) Vertical cross section of vertical velocity contoured at 1 m s^{-1} intervals. Solid (dashed) lines indicate upward (downward) vertical velocities. The thin solid line is the 0 m s^{-1} contour. (c) Vertical cross section of the U component of the horizontal velocity, contoured at 5 m s^{-1} intervals. Solid (dashed) lines correspond to westerly (easterly) core-relative flow. In (b) and (c), radar reflectivity is shaded; light shading, 5–25 dBZ; dark shading, 26–35 dBZ; no shading, 36–45 dBZ; black shading, greater than 45 dBZ. PC1 and PC2 indicate precipitation cores discussed in the text.

mensional; however, some along-front variability was apparent. For example, the V field shows two prefrontal jet maxima immediately ahead of the shear zone at 1350. The first and most intense maximum was located at the northern end of PC5 and extended northward ahead of PC4. The second maximum was near the northern end of PC3. These maxima resided primarily ahead and northward of locations where the U convergence zone bulged forward ($Y = -20$ and -72 km). These bulges in U were associated with zones of enhanced postfrontal westerly flow behind PC3 and PC5. Furthermore, the orientation of the V wind-shift zone between the southern bulge ($Y = -70$) and the southern end of the northern bulge ($Y = -40$) was such that $\partial V/\partial Y > 0$ in PC4 and near zero in PC3 and PC5. Therefore, while U was convergent everywhere along the front, V was locally divergent near PC4. One can postulate, then, that the dissipation of PC4 was associated with a change in the orientation of the V wind-shift zone from north–south at some earlier time to north–northwest–south–southeast by 1350. Section 5 provides evidence that this evolution was caused in part by the upstream influence of the orography.

By 1408 (Fig. 14b), the U field shows even greater along-front variability. The southern bulge at the northern end of PC5 intensified and a new bulge formed near the remnants of PC4. The V field (Fig. 14c) shows three prefrontal jet maxima, each associated with a bulge in the U field. Interestingly, the V wind-shift (cyclonic shear) zone exhibited much less along-front variability in shape than the U convergence zone.

The vertical structure across PC3 at 1408 is shown in Fig. 15. The reflectivity field shows an intense precipitation core with reflectivities exceeding 45 dBZ. The 25-dBZ contour extended vertically to 4–5 km, compared to 8–9 km in much of the convective band (Fig. 9). The echo depth of this NCFR (9 km) was greater than NCFRs observed previously, which had echo depths generally less than 3–6 km (Browning and Harrold 1970; Carbone 1982; Hobbs and Persson 1982; Roux et al. 1993). The intensity of reflectivity was less than that for the NCFR over land documented by Carbone (1982), in which reflectivities exceeded 50 dBZ, but comparable to reflectivities observed by Hobbs and Persson (1982) and Roux et al. (1993).

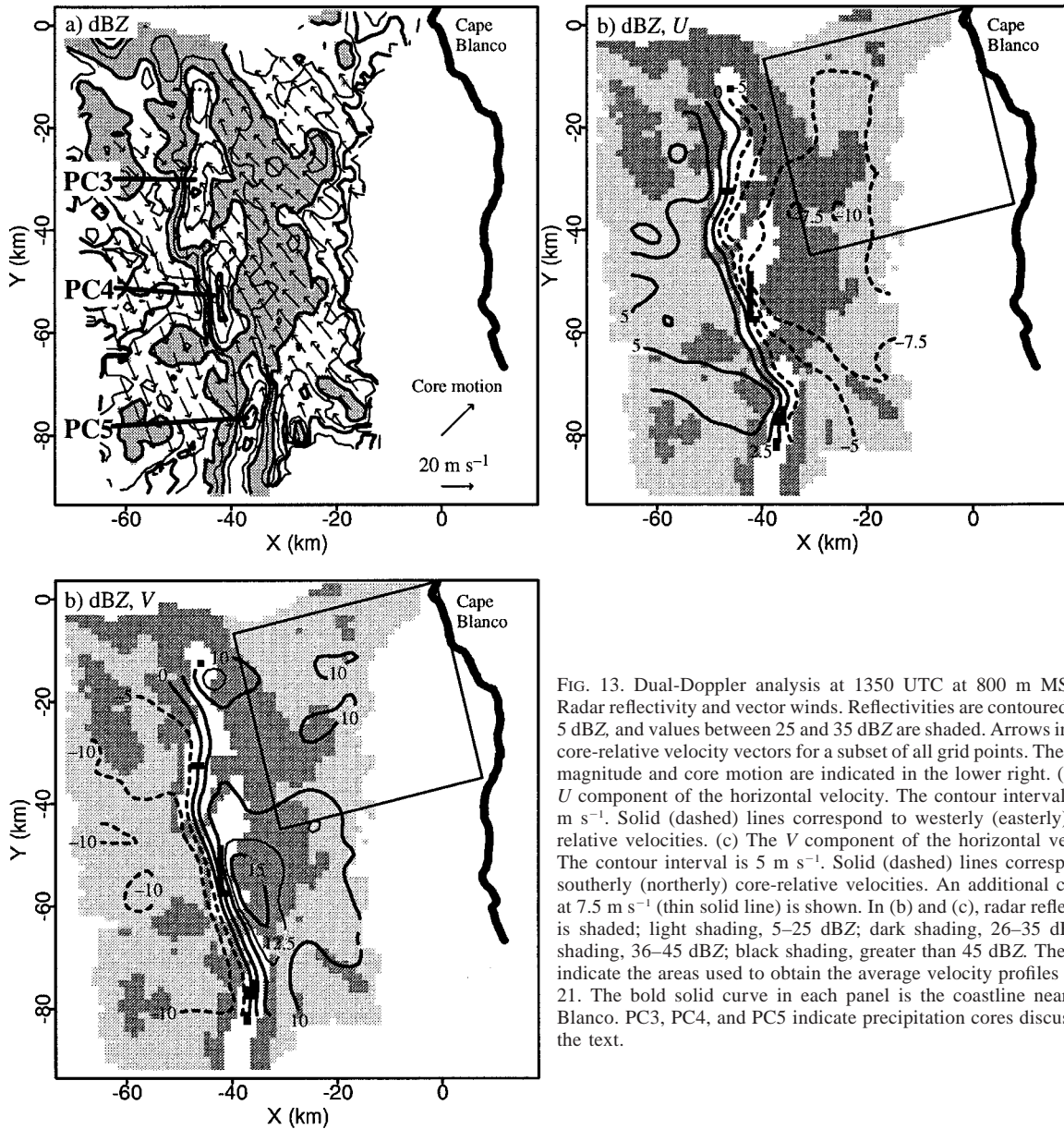


FIG. 13. Dual-Doppler analysis at 1350 UTC at 800 m MSL. (a) Radar reflectivity and vector winds. Reflectivities are contoured every 5 dBZ, and values between 25 and 35 dBZ are shaded. Arrows indicate core-relative velocity vectors for a subset of all grid points. The vector magnitude and core motion are indicated in the lower right. (b) The U component of the horizontal velocity. The contour interval is 2.5 m s⁻¹. Solid (dashed) lines correspond to westerly (easterly) core-relative velocities. (c) The V component of the horizontal velocity. The contour interval is 5 m s⁻¹. Solid (dashed) lines correspond to southerly (northerly) core-relative velocities. An additional contour at 7.5 m s⁻¹ (thin solid line) is shown. In (b) and (c), radar reflectivity is shaded; light shading, 5–25 dBZ; dark shading, 26–35 dBZ; no shading, 36–45 dBZ; black shading, greater than 45 dBZ. The boxes indicate the areas used to obtain the average velocity profiles in Fig. 21. The bold solid curve in each panel is the coastline near Cape Blanco. PC3, PC4, and PC5 indicate precipitation cores discussed in the text.

The resolved updraft in Fig. 15b was collocated with the precipitation core and had maximum amplitude (approximately 6 m s⁻¹) near 3 km, suggestive of forced ascent at the leading edge of the density current. The resolved updraft magnitudes are similar to several previous observations (Browning and Harold 1970; Hobbs and Persson 1982; Roux et al. 1993) but are much less than those described by Carbone (1982), whose analysis resolved motions on scales of 2–3 km versus 8–10 km for the airborne Doppler analysis. Updrafts in the gaps between precipitation cores (not shown), including PC4 at 1408, were weak and disorganized since the core-relative prefrontal flow

was approximately parallel to the orientation of the density current.

The U velocity field across PC3 (Fig. 15c) shows an approximately 4-km-deep layer of easterly core-relative inflow topped by a layer of strong westerly flow ahead of the front ($X > -15$ km). The easterly inflow was strong near the surface and also at the 3-km level. The inflow rose over the front but then stagnated there in a core-relative sense as the cross-frontal flow at mid-to-upper levels above the cold air was very weak. The postfrontal westerly flow was maximum near the surface, in contrast to the elevated westerly flow observed offshore behind the convective band.

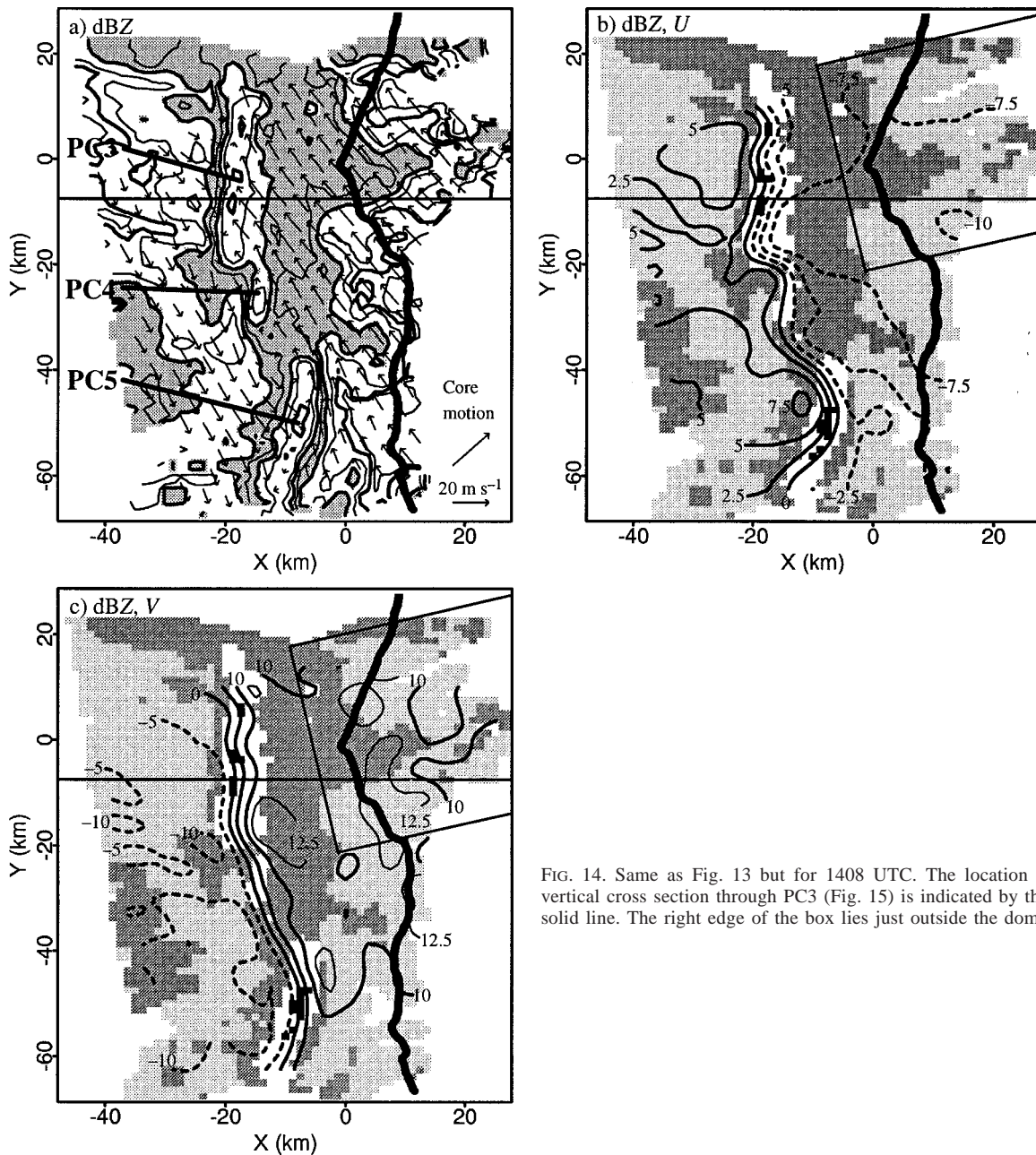


FIG. 14. Same as Fig. 13 but for 1408 UTC. The location of the vertical cross section through PC3 (Fig. 15) is indicated by the thin solid line. The right edge of the box lies just outside the domain.

2) KINEMATIC CHARACTERISTICS REVEALED BY CFADS

Figures 11c–f show the CFADs for the core-relative velocities U and V at 1350 and 1408. Above 3 km (Figs. 11c,e), the distributions of U are quite narrow. The distribution is bimodal below 3 km, as at 0917, but at 1350 and 1408 the U CFADs show the low-level westerly flow decreasing with height with the maximum westerly flow near the surface.

CFADs of the along-front velocities (Figs. 11d,f) show that significant changes occurred after 0917. By

1350 and 1408, the distributions above 3 km narrowed somewhat and shifted to larger values, particularly in the 3–7-km layer. The shift to larger values was associated with the increase in the large-scale southerly flow by 1200 (Fig. 2b and 3b) and the appearance by 1350 and 1408 of a strong southerly jet at midlevels ahead of the front (Fig. 15d). The origin of this jet is undetermined. Below 3 km, the distributions were bimodal, as at 0917, but the gap between the two modes had increased substantially as the prefrontal flow increased by about 5 m s^{-1} and the flow behind the front became

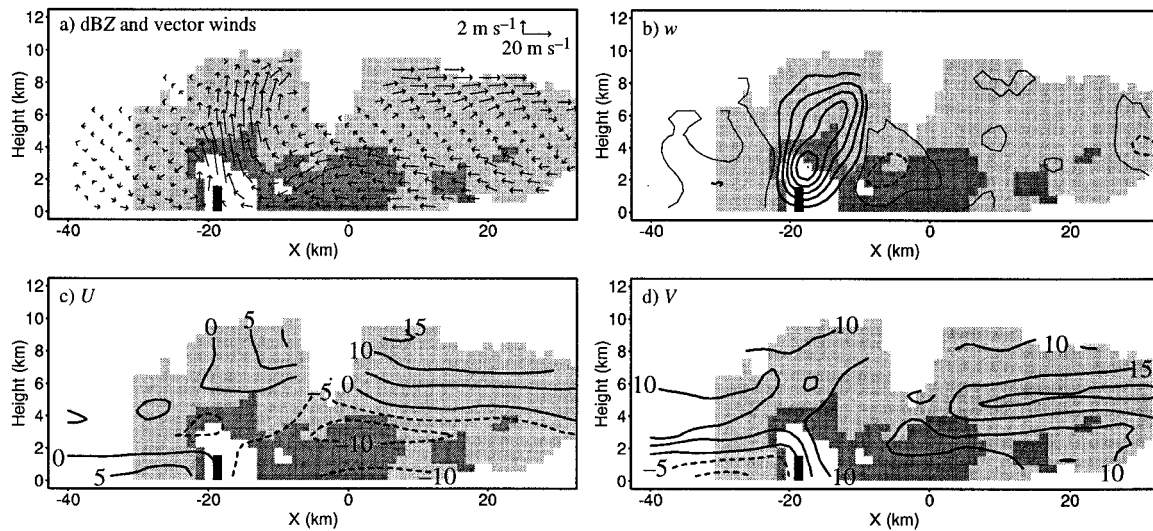


FIG. 15. Vertical cross sections at $Y = -7.5$ km at 1408 UTC (Fig. 14). Radar reflectivity is shaded; light shading, 5–25 dBZ; dark shading, 26–35 dBZ; no shading, 36–45 dBZ; black shading, greater than 45 dBZ. (a) Core-relative circulation vectors. The magnitudes of the horizontal and vertical components are indicated in the upper-right corner. (b) Vertical velocity w contoured at 1 m s^{-1} intervals. Solid (dashed) lines indicate upward (downward) vertical velocities. The thin solid line is the 0 m s^{-1} contour. (c) The U and (d) V components of the horizontal core-relative velocity, contoured at 5 m s^{-1} intervals. Solid (dashed) lines correspond to westerly (easterly) flow in (c) and to southerly (northerly) flow in (d).

slightly more negative. This result implies a change in the mean relative vorticity of the front between the offshore and nearshore stages from $22f$ to about $29f$. Maximum gridpoint values were about $75f$. The magnitude of the relative vorticity in the IOP 3 NCFR is comparable to those reported by Browning and Harrold (1970), Hobbs and Persson (1982), Bond and Shapiro (1991), and Roux et al. (1993) but is much less than the maximum values of $100\text{--}300f$ obtained in the higher-resolution analysis of a strong NCFR over land described by Carbone (1982, 1983).

It is interesting to note that the components of the precipitation-core motion (20 m s^{-1} in a ground-relative sense in both the across- and along-front directions, 0 m s^{-1} in the core-relative frame of Fig. 11) do not correspond to the velocity modes in either the pre- or post-frontal air masses. Instead, the CFADs show that at lower levels the core motion components lie in the low-frequency velocity range between the two modes and are close to the average of the values in the two modes. Hobbs and Biswas (1979), Hobbs et al. (1980), and Hobbs and Persson (1982) found that the motion of the precipitation cores normal to the front corresponded to the velocity of the front. The CFADs for V confirm Hobbs and Persson's (1982) observations that the motion of the precipitation cores along the front also corresponded approximately to the mean of the velocities in the pre- and postfrontal air masses. Low-level velocities corresponding to the core motion components were found only within the frontal zone and were observed very infrequently.

3) MECHANISMS FOR ALONG-FRONT VARIABILITY

Previous studies have tried to explain the along-front variability in NCFRs in terms of gravity currents and hydrodynamic instability associated with strong shear of the along-front winds. Carbone (1982), Hobbs and Persson (1982), Parsons and Hobbs (1983b), Parsons et al. (1987), and Parsons (1992) have shown that NCFRs behave much like density currents. Hobbs and Persson (1982) and Parsons and Hobbs (1983b) compared the along-front variability in NCFRs to lobes and clefts observed in laboratory tank experiments of gravity currents (Simpson 1969, 1972). The forward-sloping wind-convergence zones in the NCFRs in these studies and their similarity to those in the gravity currents were thought to be indicative of a gravity current mechanism for the generation of along-front variability. Parsons and Hobbs (1983b) suggested that an argument against the gravity current mechanism is that the expected wavelengths based on gravity current theory are much smaller than the often observed wavelengths of greater than 15 km.

Matejka et al. (1980), Carbone (1982), Hobbs and Persson (1982), and Parsons and Hobbs (1983b) suggested that hydrodynamic instability associated with horizontal wind shear across the front might be responsible for the along-front variability. Rayleigh (1945) and Haurwitz (1949) have shown that when a shear zone is represented by a constant shear, wavelengths less than $5W$ (W is the width of shear zone) were stable while wavelengths of $8W$ experienced the maximum growth rates. The phase speed of the wave was equal to the

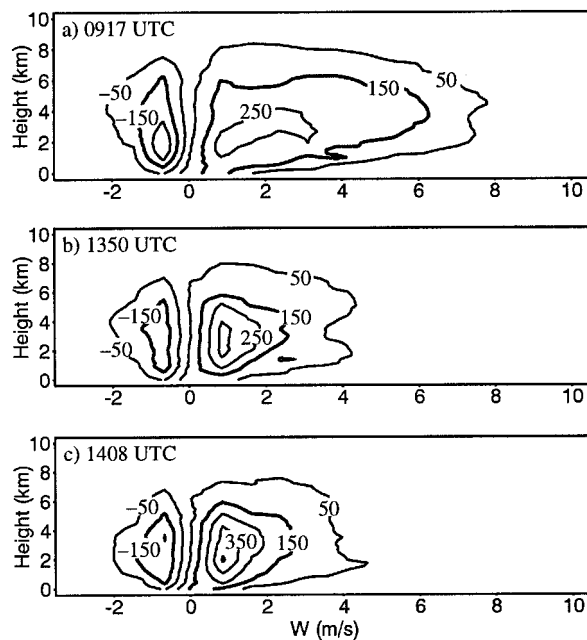


FIG. 16. Vertical mass transport CFADs. The bin size is 1 m s^{-1} and the vertical grid increment is 500 m . The contour interval is 100 Gg s^{-1} .

average of the velocities on each side of the shear zone. Based on the V fields at 1350 and 1408, the width of the shear zone was $4\text{--}8 \text{ km}$, suggesting maximum growth rates for wavelengths between 32 and 64 km . If we assume that the length scales of the precipitation cores were determined by the wavelength of a hydrodynamic instability, then the wavelength can be defined as the distance between the northern ends of the precipitation cores. At 1350, the approximate wavelength was 27 km , while at 1408, because of the dissipation of PC4, the wavelength was 54 km . The observed wavelengths are near or within the range of values expected from theory. As shown in the CFADs for V (Fig. 11), the velocity of the cores along the front was approximately equal to the average of the velocities in the pre- and postfrontal air masses, as expected from the theoretical considerations.

Moore (1985) investigated the coupling of convective and shear instabilities and showed that the most unstable wave had properties similar to precipitation cores in NCFRs. In his analysis, Moore modeled the NCFR as a narrow zone with unstable stratification. The unstable stratification was used to represent the effects of moisture on stability. For the case with strong wind shear in this unstably stratified zone (see Moore's Fig. 15), which was 5 km wide, the solution was composed of a combination of a gravity wave mode and a shear-gravity wave mode whose features were reminiscent of NCFRs. Updraft regions (taken to represent precipitation cores) exhibited anticyclonic axis rotations of approximately 30° relative to the shear zone, in good agreement with observational studies (Hobbs and Biswas 1979; Hobbs

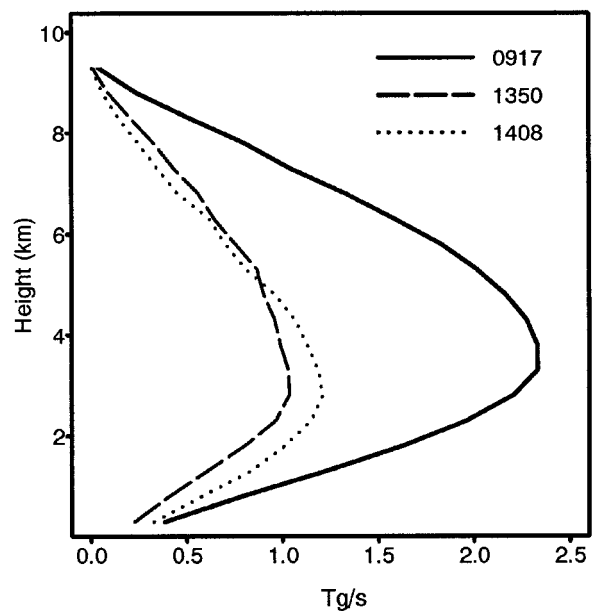


FIG. 17. Mass flux (Tg s^{-1}) for the indicated dual-Doppler volumes.

and Persson 1982). The horizontal winds, when examined in a reference frame with the Y axis oriented along the updraft axis, indicated regions of stronger westerly flow behind the precipitation cores (updraft cores) and stronger southerly flow at the northern ends of the precipitation cores. This pattern is very similar to the patterns of westerly flow and prefrontal jet maxima along the NCFR in Figs. 13 and 14 and suggests that the along-front variability may be the result of the interaction of convective and shear instabilities.

4) VERTICAL MASS TRANSPORTS AND IMPLICATIONS FOR PRECIPITATION PROCESSES

Vertical mass transport CFADs for 0917, 1350, and 1408 are shown in Fig. 16 and the total mass transport for each time is shown in Fig. 17. The vertical mass transport CFAD contour values are dependent on the size of the sampled echo area. Figure 18 shows the number of points for each level in the 0917, 1350, and 1408 analyses and indicates that the number of points were comparable at 0917 and 1350 and only slightly larger for the 1408 radar volume. Therefore, the contour values of vertical mass transport can be reasonably compared and inferences can be drawn on changes in the vertical mass transport with time. The differences in the vertical mass transport between the offshore convective band and the nearshore NCFR are readily apparent. The total vertical mass transport (Fig. 17) in the convective band at 0917 was approximately twice that associated with the NCFR at 1350 and 1408 and peaked at a slightly higher level. Keeping in mind the limitation on the accuracy of the vertical velocities (section 2), we see from

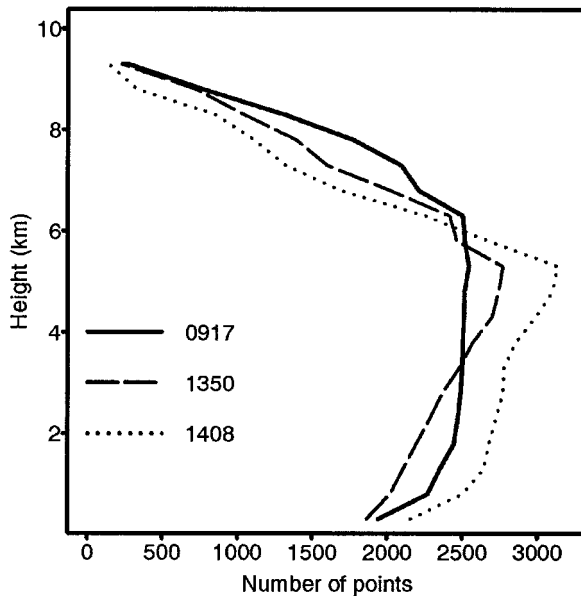


FIG. 18. Number of vertical velocity points as a function of height for the dual-Doppler volumes at 0917, 1350, and 1408 UTC.

Fig. 16 that the upward mass transport at 0917 came from a larger range of vertical velocity magnitudes (primarily from velocities between about 1 and 6 m s^{-1}), whereas at 1350 and 1408, the upward mass transport came primarily from weaker vertical velocities (less than 3 m s^{-1}). The mass transport CFADs at 1350 and 1408 evidently characterize the vertical mass transport associated with the density current in the more stable nearshore environment. Comparison of the contributions to the mass transport by updrafts less than 3 m s^{-1} at 1350 and 1408 with that at 0917, in conjunction with the vertical cross sections of dual-Doppler velocities, suggests that the density current was the dominant factor at all times but that the greater instability at 0917 led to additional mass transport by updrafts with magnitudes greater than 3 m s^{-1} . The downward mass transport at each time was generally associated with downdraft magnitudes less than 2 m s^{-1} .

The low-level reflectivities in the nearshore NCFR were of equal or greater intensity as in the offshore convective band despite the weaker vertical mass transports. The concentration of the vertical mass transport at lower levels in the nearshore NCFR (Fig. 16) suggests that coalescence growth (rain accreting cloud water and riming of precipitating ice particles) and the melting of precipitating ice particles dominated the production of precipitation (Hobbs 1978; Matejka et al. 1980; Rutledge 1989; Rutledge and Hobbs 1984; Marécal et al. 1993). The greater mass transport in a deeper layer in the convective band suggests that ice particle growth processes were more active in the convective band and a substantial fraction of the precipitation generated in the convective band was transported into the upper troposphere by the larger vertical air velocities. Once in

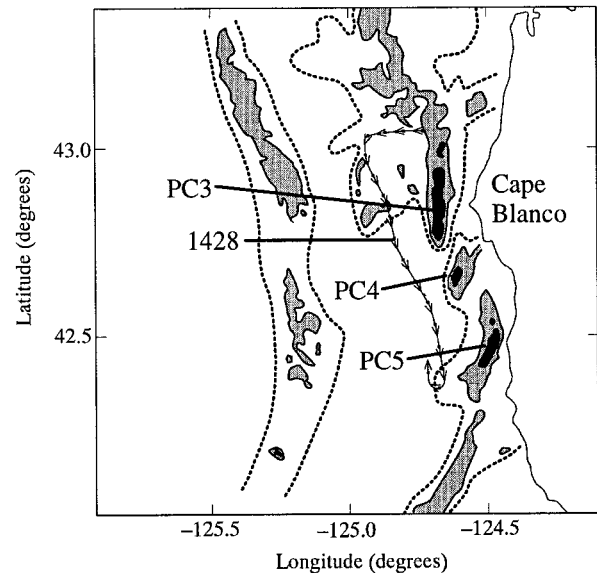


FIG. 19. Radar reflectivity composite from the lower-fuselage radar at 1428 UTC. Contour lines are drawn at 27.5, 35, and 42.5 dBZ. Reflectivities greater than 42.5 dBZ are darkly shaded and reflectivities between 35 and 42.5 dBZ are lightly shaded. The 27.5-dBZ contour lines are dashed where they were subjectively distinguished from the surrounding echo from the ocean surface. The coast is indicated by the thin solid curve on the right. A portion of the flight track is indicated by the solid line with arrows, which indicate aircraft positions at 1-min intervals. PC3, PC4, and PC5 indicate precipitation cores discussed in the text.

the upper troposphere, the strong westerly flow then transported the ice particles well ahead of the convective band to form the region of stratiform precipitation. The weaker and shallower vertical circulation in the nearshore NCFR carried far fewer hydrometeors into the upper troposphere; hence, a greater percentage of the precipitation generated by coalescence in the updrafts fell to the surface locally in the NCFR.

5. Orographic influences on the NCFR

Figure 19 shows the radar reflectivity from the lower-fuselage radar at 1428 as the NCFR moved to within 10 km of the coast. Precipitation cores PC3, PC4, and PC5 are still apparent in the reflectivity pattern. It is evident that, as the NCFR approached the coast, its shape mirrored that of the coastline to some degree. This evolution of the NCFR may have resulted from an upstream influence of the steep orography along the coast near Cape Blanco.

Studies of the upstream influence of mountain ridges have shown that an incident flow normal to the terrain is decelerated by the terrain and turned to the left by the Coriolis force upstream of the mountain ridge in the Northern Hemisphere (Smith 1979; Pierrehumbert 1984; Pierrehumbert and Wyman 1985). Such deceleration or blocking of the low-level flow has been observed to produce barrier jets along coastal mountain

regions (Overland 1984; Overland and Bond 1993, 1995). In the case of an infinitely long ridge (Pierrehumbert 1984; Pierrehumbert and Wyman 1985), the upstream deceleration of the across-mountain flow and acceleration of the along-mountain flow are primarily functions of the Rossby number $Ro = U_m/fL$ (U_m is the incident flow, L the half-width of the windward slope) and the nondimensional mountain height $h_m = NH/U_m$ (N is the Brunt-Väisälä frequency, H the mountain height). For small Ro , the upstream deceleration relative to the magnitude of the incident flow scales as $Ro h_m = (N/f)H/L$, whereas for large Ro , the upstream deceleration scales as h_m (Pierrehumbert 1984). The offshore horizontal extent of the decelerated region approximately scales as the Rossby radius of deformation $L_R = NH/f$.

Cape Blanco is located near the northern end of a quasi-two-dimensional mountain range in southern Oregon and northern California. In this region, the coastal terrain rises approximately 1.6 km within 200 km of the coast and remains high for hundreds of kilometers farther inland—that is, it resembles a broad plateau. For $N = 10^{-2} \text{ s}^{-1}$ (estimated from flight-level observations) and $f = 10^{-4} \text{ s}^{-1}$, the terrain near Cape Blanco is dynamically steep ($Ro h_m > 1$). For mean onshore flow of 10–15 m s^{-1} , typical of the conditions on 8 December 1993, $Ro \approx 1-1.5$, $h_m \approx 1-1.6$, and $L_R \approx 150 \text{ km}$. Given the large effective height ($h_m \geq 1$) and steepness ($Ro h_m > 1$) of the coastal terrain, significant deceleration of the across-shore flow and acceleration of the alongshore flow are expected.

To isolate the influences of the orography on the flow in the dual-Doppler syntheses, the horizontal velocity fields in the stratiform precipitation region ahead of the front are examined. Two assumptions are required for this analysis. First, since the mesoscale structure of the mountain range near Cape Blanco is quasi-two-dimensional, we assume that a two-dimensional conceptual framework that includes the Coriolis force (Pierrehumbert 1984; Pierrehumbert and Wyman 1985; Braun et al. 1996) is appropriate in this case. Although the presence of the cape along the coast is an obvious departure from two dimensionality, we assume that the effects of such coastline irregularities are small compared to the overall effects of the coastal mountain range. Second, we assume that the structure of the orographically influenced flow ahead of the front is steady in the ground-relative reference frame. Consequently, the dual-Doppler velocities ahead of the front are assumed to be representative of the steady response to flow over orography at the given range from the coast as the dual-Doppler area shifts closer to the coast between 1350 and 1408.

Additional support for the observational evidence of upstream orographic influence is gained through a comparison of the dual-Doppler results with the numerical calculations of Braun et al. (1996). Braun et al. (1996) used a two-dimensional terrain-following coordinate

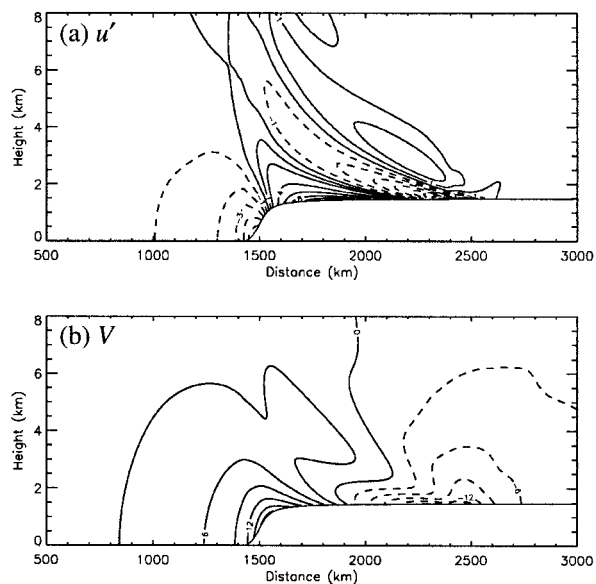


FIG. 20. (a) Perturbation across-shore velocity u' and (b) alongshore velocity V at $t = 24 \text{ h}$ associated with uniform incident flow over plateau-shaped terrain from the numerical model calculations of Braun et al. (1996). In (a), the contour interval for negative values is 1 m s^{-1} ; for positive values, contours are drawn at 2 m s^{-1} intervals with an additional contour at 1 m s^{-1} . In (b), the contour interval is 3 m s^{-1} . Solid (dashed) lines correspond to positive (negative) values. Only a portion of the total domain (3000 km in the horizontal, 14 km in the vertical) is shown.

model to calculate the response to uniform incident flow over a plateau with a height H of 1500 m and a windward slope half-width L of 78 km. This terrain profile is qualitatively similar to the terrain at the coast near Cape Blanco. The numerical model is similar to that described by Durran and Klemp (1983) with major differences being that it is Boussinesq, excludes the effects of moisture, and includes the Coriolis force and an equation for the along-mountain velocity component. The dual-Doppler results are compared to the case described by Braun et al. (1996) for which $Ro = 1.3$ and $h_m = 1.5$. The specified values of U_m , N , and f were 10 m s^{-1} , 10^{-2} s^{-1} , and 10^{-4} s^{-1} , respectively.

To aid interpretation of the dual-Doppler fields, we first describe the characteristics of the flow from the calculations of Braun et al. (1996). The perturbation across-shore ($u' = U - U_m$) and the along-shore (V) components of the flow after 24 h of model time are shown in Fig. 20. Upstream of the orography, the u' field (Fig. 20a) is characterized by a region of significantly decelerated flow, which extends offshore approximately 150 km and in the vertical through a depth slightly greater than the plateau height. Above this region, the flow is weakly accelerated. The downstream perturbations over the plateau are associated with a train of inertia-gravity waves. The alongshore flow (Fig. 20b) is characterized by a strong barrier jet above the windward slope that decays more slowly upstream than the across-shore component, in agreement with linear cal-

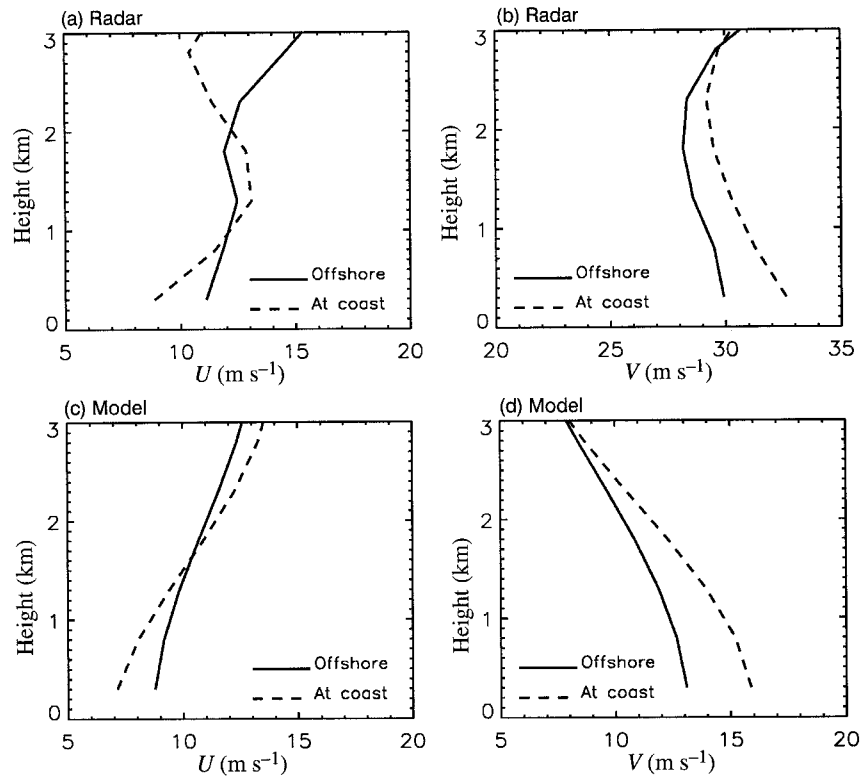


FIG. 21. Vertical profiles of the area-averaged ground-relative across-shore (a) and (c) and alongshore (b) and (d) flow. Profiles in (a) and (b) are averages obtained from the dual-Doppler data within the boxes shown in Figs. 13 and 14. The solid and dashed lines correspond to the dual-Doppler volumes located approximately 40-km offshore (1350) and at the coast (1408), respectively. Profiles in (c) and (d) are averages for similar locations relative to the terrain from the numerical model (see text for details). Only the lowest 3 km of data are shown.

culations by Pierrehumbert (1984), and extends through a depth about twice the mountain height. From our assumption that the flow upstream of Cape Blanco is approximately steady and two-dimensional, it is expected that as the dual-Doppler area shifts toward the coast, the across-shore component will decrease below 1–1.5 km and the alongshore component will increase below about 3 km. Also, based upon the magnitude of the upstream perturbations and their gradients in the model velocity fields, we expect that changes in the alongshore flow will be somewhat more apparent than changes in the across-shore flow.

The influences of the coastal orography are apparent to some degree in the low-level horizontal velocity fields from the dual-Doppler syntheses. By 1350, the NCFR was within 60 km of the coast and within the 150-km Rossby radius. Therefore, the NCFR was likely already under the upstream influence of the orography at this time. Examination of the along-front flow in Figs. 13c and 14c shows an enhancement of the flow over the terrain. At 1350, the velocities ahead of the prefrontal jet were about 10 m s⁻¹. By 1408, regions of velocities greater than 12 m s⁻¹ occurred over the coastal terrain. In the across-front flow (Figs. 13b and 14b), distinct

changes in the flow are not readily evident ahead of the front; however, the change in the shape of the convergence zone to match approximately that of the coast is suggestive of an orographic impact.

Changes in the flow can be isolated better by examining mean velocity profiles in the region ahead of PC3, where the precipitation extended over the terrain by 1408. Mean profiles of the *ground-relative* U and V (referred to as the across-shore and alongshore flow, respectively) were obtained by averaging these velocity components over the regions shown by the boxes in Figs. 13 and 14. The average profiles are shown in Figs. 21a,b. The profiles at 1350 represent mean flow characteristics approximately 10–40 km offshore, and the profiles at 1408 characterize the mean flow immediately offshore to about 20 km inland. Since significant effects of the orography are expected to occur at low levels, we restrict our focus to changes in the horizontal velocity structure below 3 km.

The profiles of the across-shore flow (Fig. 21a) indicate two layers in which the velocity changes by more than 1 m s⁻¹. In the 2–3-km layer, the across-shore flow decreases by up to 4 m s⁻¹. Inspection of vertical cross sections across PC3 at 1350 (not shown) and 1408 (Fig.

15c) suggests that this difference was associated with the strong prefrontal core-relative easterly flow near 3 km that was only partially illuminated by the radar at 1350 but became more visible to the radar as the precipitation area expanded. Since it occurs well above the mountain height, this layer of stronger core-relative easterly flow is likely associated with the frontal system. Below 1 km, the across-shore flow decreases by approximately 2 m s^{-1} near the surface and the difference between the profiles decreases with height. This change in velocity is consistent with a deceleration of the flow upstream of the orography; however, other causes for this change cannot be ruled out. Figure 21b shows a 3-km-deep layer in which the alongshore flow increased as the dual-Doppler area neared the coast. The difference is largest near the surface (3 m s^{-1}) and decreases with height. This change in the alongshore flow is consistent with the expected upstream orographic impact.

More compelling evidence for an upstream orographic impact is obtained by comparing the dual-Doppler-derived profiles with those from the model. Model profiles were obtained by averaging velocities over three adjacent grid columns at two locations: the first centered just inland of the coast at $X = 1440 \text{ km}$ (Fig. 20) and the second located 36 km upstream at $X = 1404 \text{ km}$. The 36-km separation between these model profiles is comparable to the distance in the across-shore direction separating the dual-Doppler averaging areas in Figs. 13 and 14. The model results are averaged over three grid columns to improve comparison to the area-averaged dual-Doppler data.

Profiles of the across- and alongshore components of the flow from the model are shown in Figs. 21c,d. Predicted changes in the across-shore flow are relatively small (Fig. 21c). Maximum changes occur near the surface, where the across-shore flow is reduced by nearly 2 m s^{-1} between the offshore location and the coast. The across-shore velocity change reverses sign near 1500 m, the height of the plateau. These changes in the model across-shore flow are comparable in magnitude to the changes in the dual-Doppler profiles, although velocity perturbations associated with the front (e.g., in the 2–3-km layer in Fig. 21a) complicate the comparison.

The alongshore profiles from the model (Fig. 21d) indicate an increase in the alongshore flow below 3 km between the offshore and coastal locations. The difference is largest near the surface (3 m s^{-1}) and decreases with height. While the actual shapes of the V profiles from the model and the dual-Doppler data are different, the magnitude and vertical distribution of the changes are nearly identical.

The comparison of the model and dual-Doppler wind fields together with the observed behavior of the reflectivity cores as they moved toward the coast supports the hypothesis that the NCFR was modified by the upstream influence of the coastal orography. A schematic diagram depicting the interaction of the NCFR with the

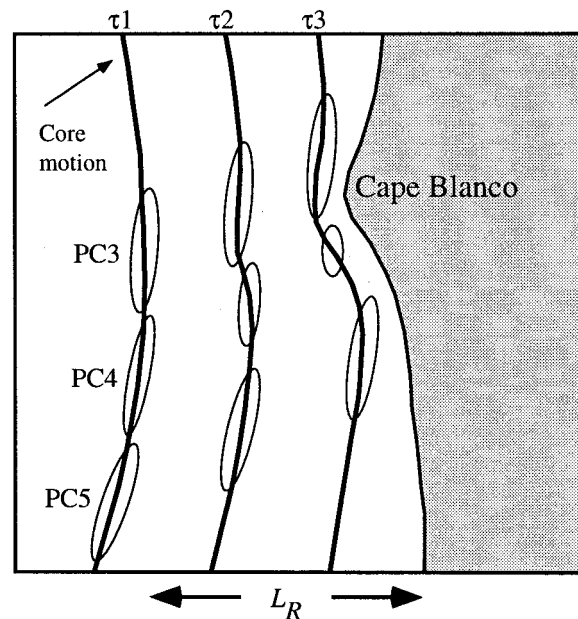


FIG. 22. Schematic depiction of the evolution of the NCFR as it came under the increasing influence of the coastal orography. Ellipses represent precipitation cores PC3, PC4, and PC5. The position of the frontal wind-shift zone and the precipitation cores are indicated at three times. The extent of the region influenced by the coastal orography is indicated by the Rossby deformation radius L_R at the bottom of the figure.

orography near Cape Blanco is shown in Fig. 22. At τ_1 , the NCFR was located a distance greater than L_R from the coast and was not yet in the region of influence of the orography. The NCFR contained several precipitation cores, each of similar length. As the NCFR approached to within a distance L_R of the coast by τ_2 , it felt the decelerating influence of the orography most strongly in the vicinity of the cape. The deceleration of the NCFR just off the cape caused an indentation in the front to develop by τ_2 . Since the wind-shift zone was associated with the front, the change in orientation of the front near PC4 was concurrently associated with a change in the orientation of the wind-shift zone (Figs. 13c and 14c), which caused the meridional component of the velocity to become locally divergent and may have led to the eventual dissipation of PC4 by τ_3 . By the time the NCFR reached the coast, its shape was deformed such that it mimicked the shape of the coastline.

6. Conclusions

a. Characteristics of an oceanic front

Past studies of North Pacific cool-season fronts, which produce most severe weather along the coastal zone of northwestern North America regardless of season, have documented various kinematic, thermodynamic, and microphysical characteristics of these storms (Nagle and Serebreny 1962; Houze et al. 1976; Hobbs

and Biswas 1979; Matejka et al. 1980; Hobbs et al. 1980; Carbone 1982, 1983; Hobbs and Persson 1982; Bond and Shapiro 1991). However, these studies (with the exception of Carbone 1982, 1983) were based on conventional radar, single-Doppler radar, and flight-level aircraft measurements and were generally unable to examine quantitatively the three-dimensional mesoscale structure of fronts far offshore and in the coastal zone. The case study presented here adds to this body of research significantly by using high-resolution airborne dual-Doppler radar to map simultaneously the detailed kinematic and radar echo structure of a strong frontal system approaching the coast of Oregon. The results of this study provide quantitative measures of certain aspects of these fronts and suggest some of the modifications such fronts may undergo as they approach the rugged coastline.

- *Frontal kinematics.* The dominant precipitation feature was a narrow cold-frontal rainband (NCFR). One of the most robust measurements provided by the airborne dual-Doppler radar is the detailed three-dimensional wind field encompassing this rainband. These data indicate a mean vertical vorticity in the frontal zone of $20\text{--}30f$ (maximum values were approximately $60\text{--}75f$) at the resolved scales of motion of $8\text{--}10$ km. The maximum values of vorticity are comparable to those found in other NCFRs (Browning and Harrold 1970; Hobbs and Persson 1982; Bond and Shapiro 1991; Roux et al. 1993) but were much weaker than the $100\text{--}300f$ noted by Carbone (1983). Maximum resolved vertical velocities were about 6 m s^{-1} at low levels along the frontal density current and greater than 10 m s^{-1} at upper levels in the offshore convective band. The density current vertical motions are similar to previous observations of NCFRs. The upward mass fluxes at the front were dominated by contributions from resolved updrafts of about $1\text{--}3\text{ m s}^{-1}$; significant contributions from stronger updrafts occurred at mid-to-upper levels in the offshore convective band.

- *Development of convection along the front.* Little is known about the pattern of deep convective cell development along cold fronts of the type studied here. This study has shown that the new convective cells systematically formed to the south of existing cells. Future studies should address what, if any, effect this development has on the position and structure of the front itself.

- *Postfrontal, cross-frontal flow.* This study raises questions about the interaction of the postfrontal, cross-frontal flow component with the convection forced by the density-current-like cold front. At locations along the NCFR where convection was deep and intense, the rear-to-front westerly current behind the NCFR was also deep and had maximum velocities just above the 0°C level, reminiscent of rear-inflow jets in squall lines. This behavior raises the question of cause and effect, which probably is best answered in the context of a high-resolution numerical model.

- *Wavelike rainbands.* Small-scale parallel rainbands oriented oblique to and in the vicinity of the NCFR were seen previously in a storm approaching the northwest coast of the United States (Houze et al. 1976). The reappearance of this phenomenon in the present case suggests that these bands are indeed characteristic of this type of oceanic frontal system.

b. Offshore versus nearshore character of the front

By virtue of observing the frontal system for several hours, beginning when the front was far out to sea and ending when the front was near the coast, we have been able to quantify observed changes in the frontal structure, which were possibly produced by changes in the low-level stability and by the interaction of the front with steep coastal topography as it came ashore.

- *Intensity.* The depth of the radar echo and magnitude of the Doppler-derived vertical velocity in the NCFR measure the intensity of the front. Both characteristics decreased as the front moved from well offshore to within about 60 km of the coast in the portion of the front observed by the aircraft radar. The cessation of deep convection and obvious signs of storm electrification near the coast suggests the stabilization of the lower troposphere as the front advanced toward the coast. Whether the weakening of the front as it approached the coast is common or not awaits further study—documentation by more observations and examination via numerical modeling.

- *Microphysical inferences.* As noted above, the radar echo depth and the maximum vertical motions decreased as the NCFR approached the coast. However, the maximum radar reflectivity at low levels did not change significantly. In other words, the rainshowers along the NCFR remained about the same intensity. The constancy of the surface rain rate as the depth of the convection decreased suggests a change in the microphysical character of the frontal clouds as they approached the coast. The anecdotal evidence of frequent lightning when the front was far offshore yet apparent absence of lightning when the storm was close to shore is further suggestive of microphysical changes. The CFADs of vertical mass transport show that the mass transport was dominated by relatively weak low-level updrafts along the frontal density current both far offshore and near shore but also show that a significant amount of additional vertical mass transport occurred in the stronger mid-to-upper-level updrafts in the offshore convective band. The concentration of vertical mass transport at low levels along the frontal density current both well offshore and near shore probably explains the similarity of the surface rain rates at both locations since most of the condensation occurred at low levels. The strong mid-to-upper-level updrafts in the offshore convective band probably increased the production and upward transport of ice particles to form the stratiform cloud and precipitation observed primarily ahead of the NCFR. Conversely, these

results imply that the convection was no longer feeding much, if any, ice into the upper-level clouds of the frontal system by the time the storm arrived at the coast, which may explain the decrease in echo depth.

• *Shape of the front.* On horizontal maps of radar reflectivity, the NCFR, which effectively marks the position of the surface front, was observed to change its shape as it approached Cape Blanco, a westward-jutting segment of the southern Oregon coastline. The terrain rises quite steeply along this portion of the coast, and the segment of the front upstream of Cape Blanco apparently was slowed down by the presence of the steep coastal terrain, resulting in a frontal shape that mirrored that of the coastline to some degree.

• *Change in the prefrontal flow.* Along with the change in shape of the NCFR as the front approached the coast, the low-level prefrontal wind parallel to the front (and also parallel to the coast) increased while the wind perpendicular to the front decreased. This behavior is suggestive of a coastal mountain influence, but it cannot be clearly separated from the large-scale baroclinic development of the frontal system and the synoptic-scale cyclone via the available observations. The relative contribution of these or other possible influences upon the front's observed behavior is probably best investigated by numerical modeling in which controlled experiments can separate orographic and baroclinic components of the flow.

Acknowledgments. The authors would like to thank Sandra Yuter, David Kingsmill, and Stacy Brodzik for assistance in the editing and synthesis of the Doppler data; Richard Rotunno and Joseph Klemp for their collaboration in the numerical modeling and comments on the manuscript; Candace Gudmundson for editing the manuscript; and Kay Dewar, David Johnson, and Michele Kruegel for helping to draft the figures. This work was supported by the Office of Naval Research Coastal Meteorology Accelerated Research Initiative (Grant N00014-95-F-0045) and was conducted in part while the lead author was a postdoctoral fellow in the Advanced Study Program at NCAR.

REFERENCES

- Biggerstaff, M. I., and R. A. Houze Jr., 1991: Kinematic and precipitation structure of the 10–11 June 1985 squall line. *Mon. Wea. Rev.*, **119**, 3035–3065.
- Blier, W., and R. M. Wakimoto, 1995: Observations of the early evolution of an explosive oceanic cyclone during ERICA IOP 5. Part I: Synoptic overview and mesoscale frontal structure. *Mon. Wea. Rev.*, **123**, 1288–1310.
- Bond, N. A., and R. G. Fleagle, 1988: Prefrontal and post-frontal boundary-layer processes over the ocean. *Mon. Wea. Rev.*, **116**, 1257–1273.
- , and M. A. Shapiro, 1991: Polar lows over the Gulf of Alaska in conditions of reverse shear. *Mon. Wea. Rev.*, **119**, 551–572.
- Braun, S. A., R. Rotunno, and J. B. Klemp, 1996: On the interaction of cold fronts with coastal orography. Preprints, *Seventh Conf. on Mesoscale Processes*, Reading, United Kingdom, Amer. Meteor. Soc., 348–351.
- Browning, K. A., 1971: Radar measurements of air motion near fronts. *Weather*, **26**, 320–340.
- , and T. W. Harrold, 1970: Air motion and precipitation growth at a cold front. *Quart. J. Roy. Meteor. Soc.*, **96**, 369–389.
- , and C. W. Pardoe, 1973: Structure of low-level jet streams ahead of mid-latitude cold fronts. *Quart. J. Roy. Meteor. Soc.*, **99**, 619–638.
- , F. F. Hill, and C. W. Pardoe, 1974: Structure and mechanism of precipitation and the effect orography in a wintertime warm sector. *Quart. J. Roy. Meteor. Soc.*, **100**, 309–300.
- Carbone, R. E., 1982: A severe frontal rainband. Part I: Stormwide hydrodynamic structure. *J. Atmos. Sci.*, **39**, 258–279.
- , 1983: A severe frontal rainband. Part II: Tornado parent vortex circulation. *J. Atmos. Sci.*, **40**, 2639–2654.
- Durrán, D. R., and J. B. Klemp, 1983: A compressible model for the simulation of moist mountain waves. *Mon. Wea. Rev.*, **111**, 2341–2361.
- Frush, C. L., P. H. Hildebrand, and C. Walther, 1986: The NCAR airborne Doppler radar. Part II: System design considerations. Preprints, *23d Conf. on Radar Meteorology*, Snowmass, CO, Amer. Meteor. Soc., 151–154.
- Haurwitz, B., 1949: The instability of wind discontinuities and shear zones in planetary atmospheres. *J. Meteor.*, **6**, 200–206.
- Hertzman, O., P. V. Hobbs, and J. D. Locatelli, 1988: Mesoscale and microscale structure and organization of clouds and precipitation in midlatitude cyclones. XVI: Three-dimensional airflow and vertical velocity budget for a warm front. *J. Atmos. Sci.*, **45**, 3650–3666.
- Hildebrand, P. H., 1989: Airborne Doppler radar accuracy. Preprints, *24th Conf. on Radar Meteorology*, Tallahassee, FL, Amer. Meteor. Soc., 585–588.
- Hill, F. F., K. A. Browning, and M. J. Bader, 1981: Radar and rain gauge observations of orographic rain over southern Wales. *Quart. J. Roy. Meteor. Soc.*, **107**, 643–670.
- Hobbs, P. V., 1978: Organization and structure of clouds and precipitation on the mesoscale and microscale in cyclonic storms. *Rev. Geophys. Space Phys.*, **16**, 741–755.
- , and K. R. Biswas, 1979: The cellular structure of narrow cold-frontal rainbands. *Quart. J. Roy. Meteor. Soc.*, **105**, 723–727.
- , and P. O. G. Persson, 1982: The mesoscale and microscale structure and organization of clouds and precipitation in midlatitude cyclones. V: The substructure of narrow cold-frontal rainbands. *J. Atmos. Sci.*, **39**, 280–295.
- , R. A. Houze Jr., and T. J. Matejka, 1975: The dynamical and microphysical structure of an occluded frontal system and its modification by orography. *J. Atmos. Sci.*, **32**, 1542–1562.
- , T. J. Matejka, P. H. Herzegh, J. D. Locatelli, and R. A. Houze Jr., 1980: The mesoscale and microscale structure and organization of clouds and precipitation in midlatitude cyclones. I: A case study of a cold front. *J. Atmos. Sci.*, **37**, 568–596.
- Houze, R. A., Jr., P. V. Hobbs, K. R. Biswas, and W. M. Davis, 1976: Mesoscale rainbands in extratropical cyclones. *Mon. Wea. Rev.*, **104**, 868–878.
- , —, M. I. Biggerstaff, and B. F. Smull, 1989: Interpretation of Doppler weather radar displays in midlatitude mesoscale convective systems. *Bull. Amer. Meteor. Soc.*, **70**, 608–619.
- James, P. K., and K. A. Browning, 1979: Mesoscale structure of line convection at surface cold fronts. *Quart. J. Roy. Meteor. Soc.*, **105**, 371–382.
- Jorgensen, D. P., and J. D. DuGranrut, 1991: A dual-beam technique for deriving wind fields from airborne Doppler radar. Preprints, *25th Int. Conf. on Radar Meteorology*, Paris, France, Amer. Meteor. Soc., 458–461.
- , and B. F. Smull, 1993: Airborne Doppler-radar observations of vortices within bow-echo mesoscale convective systems. *Bull. Amer. Meteor. Soc.*, **74**, 2146–2157.
- , P. H. Hildebrand, and C. L. Frush, 1983: Feasibility test of an airborne pulse-Doppler meteorological radar. *J. Climate Appl. Meteor.*, **22**, 744–757.
- Leise, J. A., 1981: A multidimensional scale-telescoped filter and

- data extension package. NOAA Tech. Memo. WPL-82, 20 pp. [NTIS PB82-164104.]
- Marécal, V., D. Hauser, and F. Roux, 1993: The 12/13 January 1988 narrow cold-frontal rainband observed during MFD/FRONTS 87. Part II: Microphysics. *J. Atmos. Sci.*, **50**, 975–998.
- Marks, F. D., Jr., and R. A. Houze Jr., 1987: Inner core structure of Hurricane Alicia from airborne Doppler-radar observations. *J. Atmos. Sci.*, **44**, 1296–1317.
- Matejka, T. J., R. A. Houze Jr., and P. V. Hobbs, 1980: Microphysics and dynamics of clouds associated with mesoscale rainbands in extratropical cyclones. *Quart. J. Roy. Meteor. Soc.*, **106**, 29–56.
- Mohr, C. G., and L. J. Miller, 1983: CEDRIC—A software package for Cartesian space editing, synthesis, and display of radar fields under interactive control. Preprints, *21st Conf. on Radar Meteorology*, Edmonton, AB, Canada, Amer. Meteor. Soc., 559–574.
- Moore, G. W. K., 1985: The organization of convection in narrow cold-frontal rainbands. *J. Atmos. Sci.*, **42**, 1777–1791.
- Nagle, R. E., and S. M. Serebreny, 1962: Radar precipitation echo and satellite cloud observations of a maritime cyclone. *J. Appl. Meteor.*, **1**, 279–295.
- Neiman, P. J., M. A. Shapiro, and L. S. Fedor, 1993: The life cycle of an extratropical marine cyclone. Part II: Mesoscale structure and diagnostics. *Mon. Wea. Rev.*, **121**, 2177–2199.
- O'Brien, J. E., 1970: Alternative solutions to the classical vertical velocity problem. *J. Appl. Meteor.*, **9**, 197–203.
- Overland, J. E., 1984: Scale analysis of marine winds in straits and along mountainous coasts. *Mon. Wea. Rev.*, **112**, 2530–2534.
- , and N. A. Bond, 1993: The influence of coastal orography: The Yakutat storm. *Mon. Wea. Rev.*, **121**, 1388–1397.
- , and —, 1995: Observations and scale analysis of coastal wind jets. *Mon. Wea. Rev.*, **123**, 2934–2941.
- Oye, R., and R. E. Carbone, 1981: Interactive Doppler editing software. Preprints, *20th Conf. on Radar Meteorology*, Boston, MA, Amer. Meteor. Soc., 683–689.
- Parsons, D. B., 1992: An explanation for intense frontal updrafts and narrow cold-frontal rainbands. *J. Atmos. Sci.*, **49**, 1810–1825.
- , and P. V. Hobbs, 1983a: The mesoscale and microscale structure and organization of clouds and precipitation in midlatitude cyclones. IX: Some effects of orography on rainbands. *J. Atmos. Sci.*, **40**, 1930–1949.
- , and —, 1983b: The mesoscale and microscale structure and organization of clouds and precipitation in midlatitude cyclones. XI: Comparisons between observational and theoretical aspects of rainbands. *J. Atmos. Sci.*, **40**, 2377–2397.
- , C. G. Mohr, and T. Gal-Chen, 1987: A severe frontal rainband. Part III: Derived thermodynamic structure. *J. Atmos. Sci.*, **44**, 1616–1631.
- Pierrehumbert, R. T., 1984: Linear results on the barrier effects of mesoscale mountains. *J. Atmos. Sci.*, **41**, 1356–1367.
- , and B. Wyman, 1985: Upstream effects of mesoscale mountains. *J. Atmos. Sci.*, **42**, 977–1003.
- Rayleigh, J. W. S., 1945: *Theory of Sound*. Vol. 2. 2d ed. Dover Publications, 504 pp.
- Rinehart, R. E., 1991: *Radar for Meteorologists*. 2d ed. University of North Dakota, 334 pp.
- Roux, F., V. Marécal, and D. Hauser, 1993: The 12/13 January 1988 narrow cold-frontal rainband observed during MFD/FRONTS 87. Part I: Kinematics and thermodynamics. *J. Atmos. Sci.*, **50**, 951–974.
- Rutledge, S. A., 1989: A severe frontal rainband. Part IV: Precipitation mechanisms, diabatic processes, and rainband maintenance. *J. Atmos. Sci.*, **46**, 3570–3594.
- , and P. V. Hobbs, 1984: The mesoscale and microscale structure and organization of clouds and precipitation in midlatitude cyclones. XII: A diagnostic modeling study of precipitation development in narrow cold frontal rainbands. *J. Atmos. Sci.*, **41**, 2949–2972.
- Simpson, J. E., 1969: A comparison between laboratory and atmospheric density currents. *Quart. J. Roy. Meteor. Soc.*, **95**, 758–765.
- , 1972: Effects of the lower boundary on the head of a gravity current. *J. Fluid Mech.*, **53**, 759–768.
- Smith, R. B., 1979: The influence of mountains on the atmosphere. *Advances in Geophysics*, Vol. 21, Academic Press, 87–230.
- Smull, B. F., and R. A. Houze Jr., 1985: A midlatitude squall line with a trailing region of stratiform rain: Radar and satellite observations. *Mon. Wea. Rev.*, **113**, 117–133.
- , and —, 1987: Rear inflow in squall lines with trailing stratiform precipitation. *Mon. Wea. Rev.*, **115**, 2689–2889.
- Wakimoto, R. M., W. Blier, and C. Liu, 1992: On the frontal structure of an explosive oceanic cyclone: Airborne radar observations of ERICA IOP 4. *Mon. Wea. Rev.*, **120**, 1135–1155.
- , N. T. Atkins, and C. Liu, 1995: Observations of the early evolution of an explosive oceanic cyclone during ERICA IOP 5. Part II: Airborne Doppler analysis of the mesoscale circulation and frontal structure. *Mon. Wea. Rev.*, **123**, 1311–1327.
- Weisman, M. L., 1992: The role of convectively generated rear-inflow jets in the evolution of long-lived mesoconvective systems. *J. Atmos. Sci.*, **49**, 1826–1847.
- Yuter, S. E., and R. A. Houze Jr., 1995a: Three-dimensional kinematic and microphysical evolution of Florida cumulonimbus. Part II: Frequency distributions of vertical velocity, reflectivity, and differential reflectivity. *Mon. Wea. Rev.*, **123**, 1941–1963.
- , and —, 1995b: Three-dimensional kinematic and microphysical evolution of Florida cumulonimbus. Part III: Vertical mass transport, mass divergence, and synthesis. *Mon. Wea. Rev.*, **123**, 1964–1983.